Chem Soc Rev

Photoluminescence imaging of Zn2+ in living systems

Journal:	*Chemical Society Reviews*
Manuscript ID:	CS-REV-01-2015-000005.R1
Article Type:	Review Article
Date Submitted by the Author:	03-Jan-2015
Complete List of Authors:	Chen, Yuncong; Nanjing University, State Key Laboratory of Coordination Chemistry Yang, Bai; Nanjing University, State Key Laboratory of Coordination Chemistry Han, Zhong; Nanjing University, State Key Laboratory of Coordination Chemistry He, Weijiang; Nanjing University, School of Chemistry and Chemical Engineering Guo, Zijian; Nanjing University, Coordination Chemistry Institute

Cite this: DOI: 10.1039/c0xx00000x

www.rsc.org/xxxxxx

ARTICLE TYPE

Photoluminescence imaging of Zn^{2+} in living systems

Yuncong Chen,[a] Yang Bai[a], Zhong Han[a], Weijiang He*[a] and Zijian Guo*[a]

Received (in XXX, XXX) Xth XXXXXXXXX 20XX, Accepted Xth XXXXXXXXX 20XX
DOI: 10.1039/b000000x

Zn^{2+} plays essential roles in various physiological processes in living systems, and the investigation of Zn^{2+} related physiology and pathology has attracted considerable interest. Since photoluminescence (PL) imaging possesses distinct advantages such as high sensitivity and non-invasiveness, excellent temporal and spatial resolution, it has become a powerful tool for real time monitoring of Zn^{2+} distribution, uptake, and trafficking. Over the last two decades, great efforts have been devoted to PL Zn^{2+} imaging in living systems, which proved the Zn^{2+} fluctuations in physiological processes and the temporal-spatial distribution of labile Zn^{2+} as well as the localization of labile Zn^{2+} pools. Advances in PL techniques such as fluorescence microscopy, confocal fluorescence microscopy, two photon fluorescence microscopy, lifetime based techniques and luminescence optical imaging system have made remarkable contributions in tackling major challenges in Zn^{2+} PL imaging. With the rational design and proper use of fluorescent sensors, Zn^{2+} imaging in various cells lines, organelles, tissues, organs and living animals have been realized, which was shown to be crucial in elucidating the biological and physiological roles of labile Zn^{2+}.

1. Introduction

Zinc is the second most abundant transition metal ion in the human body following iron. The content of total zinc in an adult human body is estimated to be 2-3 g, and long term insufficient intake of zinc will cause stunted growth of children.[1] Total zinc concentration in a mammalian cell is reported in several hundreds of micromolar range.[2,3] Most biological Zn^{2+} is tightly bound to proteins and enzymes, and "labile" Zn^{2+} which is also often denoted as "free", "mobile", "chelatable", "exchangeable", "accessible" Zn^{2+} in the literature, is quite low in general. Nevertheless, several millimolar concentration of Zn^{2+} could be attained in some organisms or tissues such as hippocampus of the brain,[4] pancreas[5] and prostates[6]. The homeostasis of Zn^{2+} in living systems is exquisitely regulated by three classes of proteins: Zn^{2+} buffer proteins, Zn^{2+} transporters and Zn^{2+} sensor proteins. The thiol-rich metallothioneins (MTs) which could bind a large number of Zn^{2+} and release Zn^{2+} in the presence of oxidative stress, [7,8,9] act as Zn^{2+} buffer and storage proteins. Zn^{2+} transporters such as ZnT and ZIP proteins have opposite functions and control the cellular uptake and excretion of Zn^{2+}.[10,11] It is reported that maternally derived ZIP6 and ZIP10 facilitate the transition from oocyte to egg by influx necessary zinc during meiotic maturation. [12] Zn^{2+} sensor proteins are sensitive to the intracellular labile Zn^{2+} fluctuation.[13,14,15] These proteins regulate transcription factors to express MTs and/or Zn^{2+} transporters and sustain Zn^{2+} homeostasis.[16]

Labile Zn^{2+} in living systems has been proposed to initiate transient signals that stimulate various physiological processes.[17,18] Substantial evidence has demonstrated that Zn^{2+} plays an important role in apoptosis,[19] and both labile Zn^{2+} regulation and Zn^{2+}-associated DNA/RNA polymerases were involved in apoptosis.[20] Labile Zn^{2+} is associated also with the regulation of gene expression and insulin secretion.[21,22]

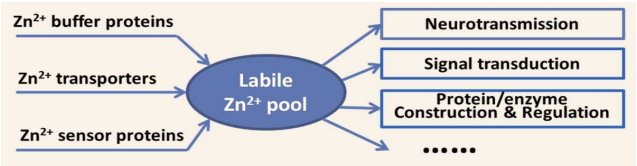

Fig. 1 Proposed scheme of Zn^{2+} homeostasis in living systems.

Moreover, labile Zn^{2+} is believed to play important neurological roles and is considered as a neurotransmitter.[23,24,25] In a complete synaptic transmission, labile Zn^{2+} ions are co-released with glutamate from synaptic vesicles of a presynaptic neuron, traverse the synaptic cleft and then arrive at a postsynaptic neuron. [26] In this signalling pathway, Zn^{2+} is recognized as a second messenger, [27] similar to Ca^{2+} in the hippocampus for long-term potentiation. Newly synthesized proteins recruit labile Zn^{2+} and convert it into bound Zn^{2+}. The bound Zn^{2+} may act as a structural cofactor in many metalloproteins, such as SOD and zinc finger family, which are key components in many transcription factors.[28,29] In addition, many hydrolytic enzymes contain Zn^{2+} in their catalytic pockets and zinc-bound water or hydroxide are recognized as excellent nucleophiles.[30,31,32,33] On the other hand, the disruption of Zn^{2+} homeostasis has been found to be associated with many neurological disorders such as Alzheimer's disease, Parkinson's disease, epilepsy and amyotrophic lateral sclerosis.[34,35,36]

Comprehensive understanding of the distribution, uptake, and

trafficking of labile Zn^{2+} in living systems ranging from subcellular to model animals is essential for the understanding of the related biological processes. Therefore, the development of non-invasive detection techniques for real-time imaging of labile Zn^{2+} is highly demanded. With the electronic configuration of $3d^{10}4s^0$, Zn^{2+} is redox inert and invisible to most photo-spectroscopic techniques. Mass spectrometry such as secondary ion mass spectrometry (SIMS), nano-SIMS, and laser ablation coupled with ICP-MS (LA-ICPMS) are able to provide the general information of total Zn^{2+} in fixed specimens but offer little in real time Zn^{2+} monitoring.[37] Synchrotron and focused ion-beam microprobes with high-energy excitation beam are also not suitable for the living cell/tissue imaging.[38,39] Since Zn^{2+} does not quench the molecule luminescence, photoluminescence (PL) imaging techniques stand out as the most effective choices due to their high sensitivity/selectivity, excellent spatial-temporal resolution and invasiveness. After initial simple fluorescence microscopy, confocal microscopy, two photon fluorescence microscopy, fluorescence lifetime imaging microscopy (FLIM) and optical imaging technique for small animals (imaging depth up to centimetre) have been applied for Zn^{2+} imaging. Over the years, labile Zn^{2+} imaging has achieved significant progresses with the fast development of photoluminescent Zn^{2+} sensors. Readers are referred to many excellent reviews on the design of photoluminescent Zn^{2+} sensors.[40,41,42,43,44,45,46,47]

Magnetic resonance imaging (MRI) is another non-invasive molecular imaging technique, which has been frequently applied in clinical diagnosis.[48] Although this method suffers from lower sensitivity and poorer temporal-spatial resolution when compared with the PL imaging, the efforts on Zn^{2+} responsive MRI contrast agents has displayed the potential of MRI Zn^{2+} imaging.[49,50,51] Since MRI exhibits an advantage in providing three-dimensional information of opaque specimens such as a whole living animal, the future advances in MRI Zn^{2+} imaging can be anticipated. This critical review will focus on the PL imaging of labile Zn^{2+} in the biological samples. Readers who interested in Zn^{2+} responsive contrast agents for MRI are referred to recent reviews on the subject.[52]

2. PL imaging modes for Zn^{2+} in living systems

2.1 Imaging techniques and luminescent materials

Widefield fluorescence microscopy (WFM) and laser scanning confocal microscopy (LSCM) are the most widely used PL imaging techniques in life science. For WFM, the microscope is fitted with various bandpass filter sets, including an excitation filter, a dichroic mirror, and an emission filter, which are adjustable for different fluorophores. Most fluorophores can be used because of the excitation with a tuneable continuous light beam with a bandpass as large as 60 nm which might generate strong background fluorescence. In addition, the specimen is illuminated in the entire focal plane simultaneously, and the photons generated from the out-of-focus planes are also collected by the detector. Therefore, WFM usually suffers from the relatively poor resolution, and the lateral and axial resolution could be 180-250 nm and 500-700 nm respectively.[53]

This technique faces several major challenges. For example, the detected fluorescence by normal WFM imaging is the summated signals emitting from the different layers of the specimen, no longitudinal resolution was offered. Moreover, as fluorescence intensity can be affected by local sensor concentration and environments and other imaging parameters for excitation and signal detection, minor deviations in Zn^{2+} level can be masked by the changes of these factors, therefore Zn^{2+} imaging based on single emission band is hard to provide accurate quantitative information. On the other hand, autofluorescence, photobleaching and photodamage are key obstacles for imaging accuracy when excited by light of short wavelengths. Finally, the limited imaging depth due to the tissue scattering and absorption is another major problem for in vivo Zn^{2+} imaging. For sharper and deeper view of Zn^{2+} inside the specimen, both the imaging technique and Zn^{2+} sensor should be improved.

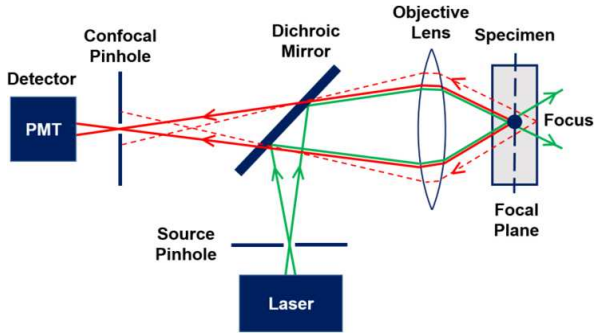

Fig. 2 Schematic representation of a laser scanning confocal microscope. It differs from a conventional fluorescence microscope with the two pinholes placed in front of the light source and in front of the photodetector which are conjugate with each other. Excitation laser light through the source pinhole is focused through the objective lens to a diffraction-limited spot in the focal plane of the specimen. Out-of-focus fluorescence is rejected by the confocal pinhole (red dashed line), while in-focus light is allowed through the pinhole (red line) and collected by the photomultiplier (PMT).

Most background fluorescence from out of the focus plane can be removed by LSCM fitted with two conjugated pinholes being placed respectively in front of the light source and detector (Fig. 2). Therefore, only the fluorescence excited on the focus point in specimen can enter into the pinhole for detection, and the pointwise scanning of focal plane leads to two-dimensional image of high contrast, since both the scattered light from the focal plane and out-of-focus light can be distinctly reduced. The improved signal-to-noise ratio (S/N) provides LSCM improved axial resolution compared to WFM, even though the theoretical axial resolution still remains the same under practical conditions. The LSCM is thus endowed with the optical sectioning ability, and stacking the images obtained at different Z-positions (upto 100 μm) leads to the reconstruction of a 3D image.[54,55] However, the number of the monochromic excitation lasers is limited, which might not match the excitation maxima of available sensors. In addition, strong laser excitation is needed because only the photons originated from the focal plane will be collected, which might promote photo-bleaching and photo-damage. Nevertheless, the development of LSCM has been considered a milestone for PL imaging, and has demonstrated great potential in cell biology studies.

Similar to the imaging of Ca^{2+} and other biochemical species, Zn^{2+} luminescence imaging is normally realized with FM and

LSCM via recoding Zn^{2+}-altered parameters of sensor luminescence, and the luminescence intensity in certain wavelength window upon the defined excitation is the most recorded parameter. Other characteristic parameters of molecule luminescence, such as lifetime, and ratio of dual emission have also been utilized to achieve the Zn^{2+} imaging. Besides the LCSM, the high-powered pulsed lasers for two photon fluorescence, the time correlated single photon counting (TCSPC) techniques for fluorescence lifetime imaging (FLIM), and optical imaging techniques for small animals, were developed to promote the Zn^{2+} imaging to offer higher S/N ratio and spatial/temporal resolution, and more accurate quantitative information. More detailed discussion will be given later in this review.

Most Zn^{2+} sensors are small molecular organic fluorophores, and those of longer excitation wavelength are more attractive, especially the near infrared (NIR) molecular sensors, two-photon (TP) excitable sensors for their promoted imaging depth for Zn^{2+} imaging in tissues and small animals, which will be discussed in detail in Section 6. Phosphorescent metal complex-based sensors have also been developed for Zn^{2+} imaging, which are powerful in avoiding the interference of autofluorescence. The most attracting advantage of these sensors is their suitability for lifetime-related imaging techniques, which will be discussed in Section 4.

Fluorescence protein (FP)-based macromolecule sensors have also been explored to provide specific advantages in Zn^{2+} imaging. They are normally adopted to construct Zn^{2+} sensors of Förster resonance energy transfer (FRET) response, favouring ratiometric Zn^{2+} sensing. Moreover, these sensors can be readily expressed in particular organelles of interest, which offers a practical way for Zn^{2+} imaging in different subcellular compartments, and this will be discussed later in subcellular Zn^{2+} imaging. Luminescent nanomaterials (Quantum dots, lanthanide-doped uperconversion luminescent particles, carbon nanotube etc.) normally exhibit high quantum yield, high photo- and chemo-stability, sharp emission band, which makes them preferable for multicolour imaging and long-term tracking. Many nanomaterials were reported with NIR emission or excitation, [56, 57, 58] and endowing these materials with Zn^{2+} sensing ability should be a reliable means to realize Zn^{2+} imaging in live animals.

2.2 Zn^{2+} imaging protocols and specimen

Photoluminescent imaging for Zn^{2+} has been investigated at different levels, from fixed or live cells to organelles, and from tissues to animal modes. Two most widely adopted imaging protocols are follows. In the first protocol, the stained specimen in rest was imaged at first, then the specimen was loaded with exogenous Zn^{2+} for imaging via direct Zn^{2+} incubation (using solution of zinc salts or Zn^{2+}/pyrithione complex) or via injection. Then, the Zn^{2+}-loaded specimen was further treated by incubation with solution of Zn^{2+} scavenger such as TPEN (*N,N,N',N'*-tetrakis(2-pyridylmethyl)ethylenediamin, a cell membrane permeable chelator to deprive intracellular Zn^{2+}) or EDTA (cell membrane impermeable to deprive intercellular Zn^{2+}) before imaging. With this rest - Zn^{2+} loading- Zn^{2+} scavenging (RLS) procedure of imaging, the Zn^{2+} imaging properties of a Zn^{2+} sensor, such as cell membrane permeability, sensing reversibility, and response dynamics in specific specimen can be revealed. In the second protocol, exogenous Zn^{2+} loading was replaced by stimulation with specific reagents such as RNS (reactive nitrogen species such as NO, S-nitrosocysteine i.e. SNOC, a precursor of NO), ROS (reactive oxygen species, such as H_2O_2), and other reagents. In this way, the endogenous Zn^{2+} level can be enhanced and monitored by the sensor. It is evident that the second protocol, rest-Zn^{2+} stimulation-Zn^{2+} scavenging (RSS) procedure, is more reliable for the evaluation of endogenous Zn^{2+}.

The specimen suitable for the current Zn^{2+} imaging techniques can be fixed cells, living cells, tissues, and animal modes. Major advances have achieved in the past two decades on intracellular Zn^{2+} imaging. However, a comprehensive understanding of Zn^{2+} physiology is far from satisfaction, and Zn^{2+} cytophysiology is still not fully understood. For example, whether or how the labile Zn^{2+} level regulates the physiological functions of different organelles is always the question to be answered. As Zn^{2+} plays important roles in the regulation of cell proliferation and apoptosis, the involvement of specific organelles in these processes warrants further investigation. Therefore, Zn^{2+} tracking in specific organelles or compartments is highly demanded. In section 5, photoluminescence Zn^{2+} imaging in subcellular level will be discussed, including the targeting strategies and the related biological imaging application.

Zn^{2+} imaging within live cell is not enough for the understanding of Zn^{2+} physiology. It remains unclear how labile Zn^{2+} is involved in the exchange of substance, energy and information between cells. The exact roles of Zn^{2+} in various tissues and organs of different physiological functions are not well defined. All these questions demand spatial and temporal information of labile Zn^{2+} in live animals. Due to the lack of proper sensors and the difficulty in live imaging, the study of Zn^{2+} imaging in mammalian animals is rare, although numerous trials have been conducted on transparent animal models such as zebrafish. With the development of NIR/TP sensors, promising progresses have been made in Zn^{2+} imaging in tissues and small animal modes, which will be discussed in section 6.

3. Intensity-based intracellular Zn^{2+} imaging

Most intracellular Zn^{2+} imaging was realized based on the measurement of PL intensity. For intensity-based Zn^{2+} imaging, both single channel imaging mode and multichannel mode have been frequently reported. The former records the fluorescence intensity from the only one detection channel, while the latter records the emission intensity from different channels or from same channel upon different excitation, and the ratio of intensity from different channels or ratio of intensity upon different excitation was calculated to give the ratiometric image. This multichannel imaging is also well known as ratiometric imaging.

3.1 Intracellular turn-on Zn^{2+} imaging: single channel imaging

For single channel imaging, Zn^{2+} luminescent sensors or probes, which undergoes the luminescence intensity change upon Zn^{2+} binding or Zn^{2+}-induced reaction, were required to show the presence of labile Zn^{2+}. The turn-on sensors, which often show a Zn^{2+}-enhanced emission, are more preferable than their turn-off counterparts for high S/N ratio. A number of small molecular sensors or probes of turn-on Zn^{2+} response have been reported. Most of them function via photo-induced electron transfer (PET):

where the luminescence of a fluorophore is quenched by PET effect and Zn^{2+} chelation blocks the PET process to restore the emission. This Zn^{2+} chelation-enhanced fluorescence is also defined as metal chelation enhanced fluorescence (MCHEF). The efficiency of PET, which regulates Zn^{2+}-induced emission enhancement factor, could be tuned via chemical modification of the fluorophore, Zn^{2+} chelator and the linker bridging the two.

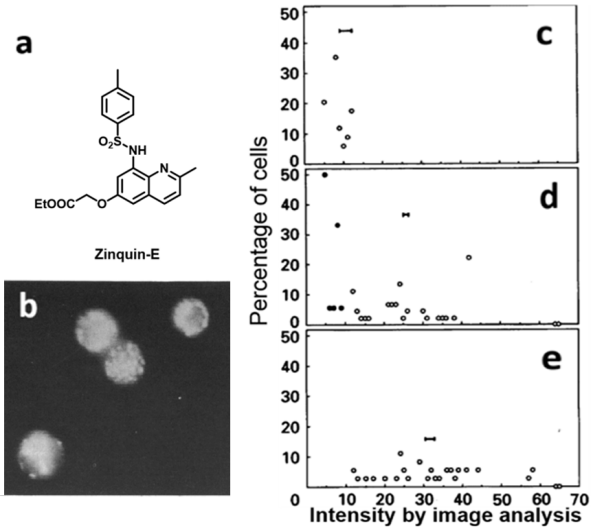

Fig. 3 (a) Chemical structure of Zinquin-E. (b) Widefield fluorescence images of CLL cells incubated with Zinquin-E. (c-e) Percentage of positive cells with fluorescence intensity. CLL cells were treated with (c) 0, (d) 1 or (e) 4 μM pyrithione and 25 μM $ZnSO_4$ (hollow circle) or no Zn^{2+} (solid circle). Adapted from ref. 59.

The first intracellular Zn^{2+} imaging in living cells was reported in a single channel model with Zinquin,[59,60] which was derived from TSQ.[61] Zinquin-E, a cell membrane permeable ester, was used for WFM. After entering the cells, Zinquin-E was hydrolysed by esterase to form Zinquin acid and retained inside cells. The diffuse and punctate fluorescence pattern, which was mainly restricted to extranuclear regions, was disclosed in this study (Fig. 3b). The RLS imaging procedure showed clearly the change of cell percentage with high fluorescence intensity and confirmed the effectiveness of Zinquin in intracellular Zn^{2+} imaging (Fig. 3c-e). Zinquin then became one of the most frequently utilized Zn^{2+} sensors for cytoplasmic Zn^{2+} real-time imaging in the 1990s.[62,63,60] This also the first time that pyrithione was confirmed directly with the ability to load exogenous Zn^{2+} into the live cells by Zn^{2+} imaging, which favors the later RLS imaging procedure for intracellular Zn^{2+} imaging.

The first generation of Zn^{2+} sensors is normally excited by UV light which can lead to severe photo-bleaching and photo-damage and decreases effective imaging time. Moreover, the autofluorescence ascribed to the UV excitation of endogenous fluorophore also interferes with single channel Zn^{2+} imaging. To overcome the disadvantage of UV excitation, second generation of Zn^{2+} sensor fluorophores with visible light excitation profiles mainly fluorescein and rhodamine derivatives have been developed in the last decade, led by Lippard, Nagano and Gee et al.

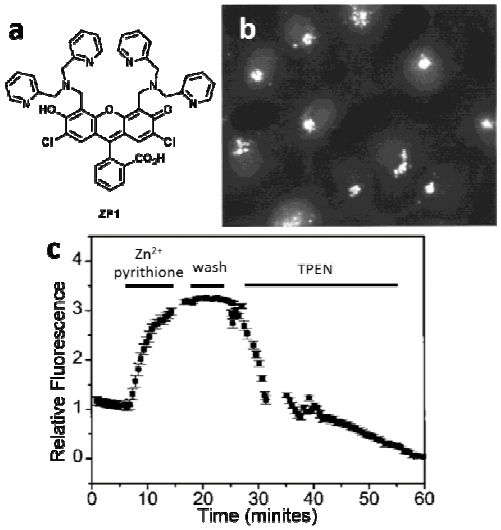

Fig. 4 (a) Chemical structure of ZP1. (b) Widefield fluorescence microscopy image of ZP1(5 μM)-loaded Cos-7 cells. (c) Fluorescence intensity analysis of ZP1-stained Cos-7 cells in (b). The cells were investigated with a RLS procedure using Zn^{2+}/pyrithione as the Zn^{2+} loader, while TPEN as the Zn^{2+} scavenger. Adapted from ref. 63.

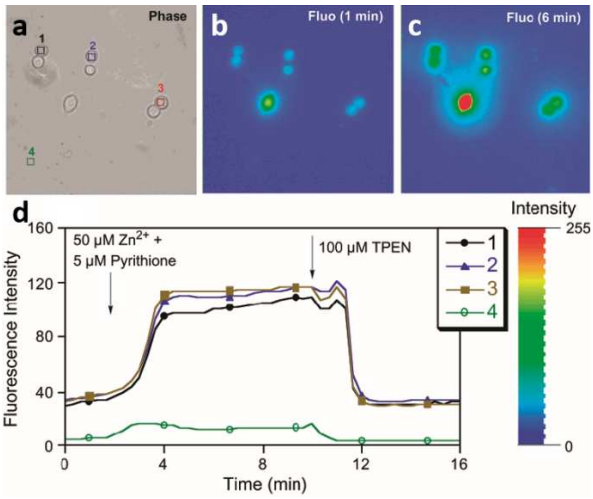

Fig. 5 (a) Bright-field and (b, c) fluorescence images of RAW 264.7 cells incubated with 10 μM ZnAF-2F DA. (d) Average fluorescence intensity of the corresponding areas (1-3, intracellular region; 4, extracellular region) changes as a function of time. The fluorescence excited at 470-490 nm was measured at 20s intervals. At 2 min, Zn^{2+}/pyrithione were added to the medium, and at 10 min 100 μM TPEN was added. Adapted from ref. 66.

Lippard reported the first example of turn-on imaging for intracellular Zn^{2+} with visible light excitation using ZP1 which contains two Zn^{2+} chelators DPA (di-2-picolylamine) in 4',5'-position of fluorescein.[64] Zn^{2+} imaging with ZP1 in Cos-7 cells displayed a bright punctate staining pattern under fluorescence microscope (Fig. 4b). The RLS imaging procedure demonstrated clearly the reversible imaging ability of ZP1 to intracellular Zn^{2+} (Fig. 4c). With prolonged imaging time (for ZP1 in Fig 4b, at least 1 hour) profiting from the visible light excitation, the RLS imaging procedure can be realized effectively in the same cells, favouring the more effective evaluation of the intracellular imaging ability of the sensors. Shortly afterwards, Nagano reported ZnAF-1 with a specific turn-on response for Zn^{2+}, in which the fluorescein was tethered with a DPA-derived chelator

in its phenyl carboxylic acid moiety.[65] Its diacetyl analogue ZnAF-2F was utilized for visualization of spatiotemporal Zn^{2+} fluctuation in macrophages via WFM imaging (Fig. 5).[66]

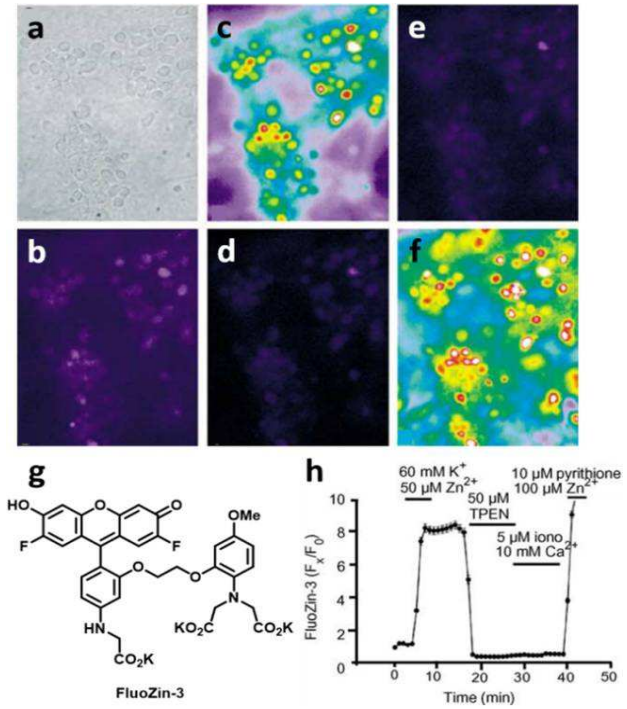

Fig. 6 (a-f) Widefield fluorescence images of neurons loaded with AM ester forms of FluoZin-3 (λ_{ex}, 488 nm, λ_{em} 520 nm). (a) Bright field image; (b) baseline fluorescence image and fluorescence image after 5 min exposure to K^+ in the presence of Zn^{2+} (c), followed by addition of TPEN (d) and after addition of ionomycin and Ca^{2+} (e) and after addition of pyrithione and Zn^{2+} (f). (g) Chemical structure of FluoZin-3; (h) Quantitative fluorescence changes upon the indicated manipulations. Adapted from ref. 68.

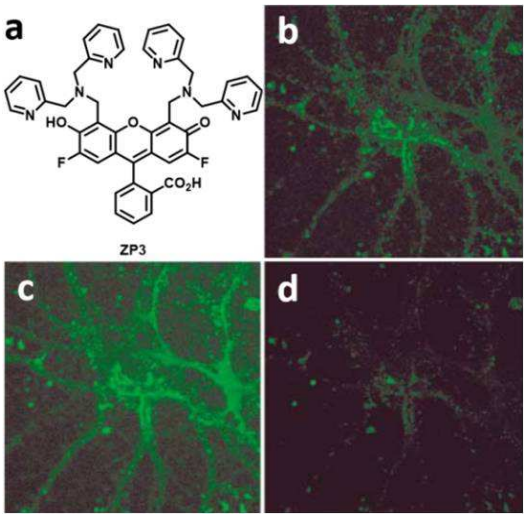

Fig. 7 (a) Chemical structure of ZP3. (b-d) Confocal fluorescence images of live hippocampal neurons labelled with ZP3. (b) Incubation of neurons with 10 μM ZP3 for 20 min at 37 °C; (c) ZP3-stained neurons loaded with 50 μM Zn^{2+}/pyrithione; (d) further treated with 50 μM TPEN. Adapted from ref. 75.

Similar fluorophore platforms were adopted by scientists of Molecular Probe, and a series of Zn^{2+} indicators with excitation window ranging from visible light to far red light were developed.[67,68] These sensors displayed large Zn^{2+}-triggered fluorescence enhancement. The intracellular fluorescence imaging in neurons loaded with AM ester forms of FluoZin-1/2/3 was carried out by inverted fluorescence microscope (Fig.6). The presence of K^+ is helpful to load exogenous Zn^{2+} into the cells, just like intracellular Zn^{2+} transport promoted by pyrithione. However, the presence of Ca^{2+} ionophore ionomycin and Ca^{2+} did not induce any fluorescence enhancement in the cells. Besides the revisable imaging ability, FluoZin-3 is suitable for long time monitoring for intracellular Zn^{2+}, just as showed by RLS imaging procedure.

Further improvement of ZP1 and ZnAF-1 has led to the development of two families of Zn^{2+} sensors, Zinpyrs (ZPs) and ZnAFs.[68,69,70,71] These sensors showed lower excitation/emission energy and higher bio–compatibility, profiting distinct intracellular Zn^{2+} imaging. An additional advantage of these sensors is their excitation matches perfectly with the 488 nm Ar laser line. This makes their LCSM imaging more practical to achieve 3D intracellular distribution patterns of Zn^{2+} other than the summated information offered by WFM imaging. In fact, the LCSM imaging for Zn^{2+} has been obtained firstly with Zinquin as an imaging agent,[72,73] yet the results suggested that the distinct photobleaching or "leaking" of the dyes might prevent the sensitive and selective Zn^{2+} measurements in cells. Moreover, the autofluorescence blurred the intracellular Zn^{2+} image distinctly. The more practical LCSM imaging was realized with these second generation Zn^{2+} sensors of visible light excitability. For examples, zinc secretion from pancreatic β-cells upon glucose stimulation was monitored with LCSM using FluoZin-3.[74] FluoZin-3 staining has also been utilized to show the punctate zinc localization enriched in the cortex of the human oocyte.[12] Intracellular Zn^{2+} imaging in live hippocampal neurons via LCSM was realized using ZP3.[75] With RLS imaging procedures, ZP3 was able to visualize endogenous Zn^{2+} in neuron with high contrast via LCSM imaging, as shown in Figs. 7b and 7d.

Inspired by the Cys_2His_2 binding motif of Zn(II) finger peptides, Lippard and coworkers developed another family of Zn^{2+} sensors, Zinspy (ZS) family, in which one pyridyl group of the Zn^{2+} chelators DPA was replaced by a thioether or thiophene.[76,77] Among these sensors, ZS5 was found to permeate into a number of immortal cell lines to realize the intracellular Zn^{2+} imaging.[77] LCSM imaging with a RLS procedure using Zn^{2+}/pyrithione or Zn^{2+}/glutamate as exogenous Zn^{2+} loading agent confirmed that ZS5 enters in both embryonic hippocampal and postnatal dentate gyrus neurons (Figs. 8b-8d) and is Zn^{2+}-responsive. Time-lapse LCSM imaging showed clearly the fluorescence increasing process upon Zn^{2+}/pyrithione incubation and the following fluorescence decrease after TPEN treatment, howing the effective temporal monitoring of intracellular Zn^{2+} by LCSM imaging (Fig. 8d). Zn^{2+} release process from Zn^{2+} buffer proteins in dentate gyrus neuron triggered by SNOC-induced nitrosative stress was also visualized (Fig. 8e).

Zn^{2+} sensors from ZnAF family exhibit low background fluorescence (Φ_{free} = 0.004-0.023) and large dynamic range upon Zn^{2+} binding (17- to 69-fold), favoring Zn^{2+} imaging application, especially LCSM imaging. Their different Zn^{2+} binding affinities can be utilized to image the variable intracellular Zn^{2+} levels. The imaging behaviors of ZnAF-2 (K_d ~2.7 nM) and ZnAF-3 (K_d

~0.79 μM) in Zn^{2+}-incubated CHO cells in the presence of pyrithione disclosed that ZnAF-2 is sensitive in visualizing Zn^{2+} increases upon incubation with 3 μM Zn^{2+},[70, 71] while ZnAF-3 is sensitive upon incubation with 30-300 μM Zn^{2+} (Fig. 9). Therefore, Zn^{2+} binding affinity of fluorescent probes is an important factor in intracellular fluorescence imaging.

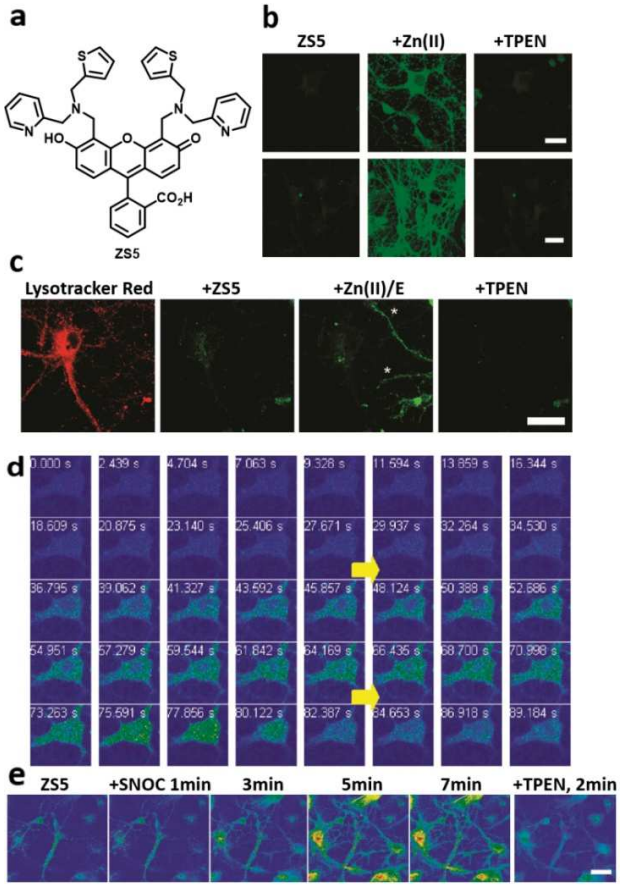

Fig. 8 (a) Chemical structure of ZS5. (b) Zn^{2+} response of ZS5 in hippocampal (upper row) and dentate gyrus (buttom row) neurons. Left panels: confocal fluorescence images of neurons treated with 10 μM ZS5. Middle panels: images of cells in left panels after addition of 50 μM Zn^{2+}/pyrithione (1:2 ratio). Right panels: images of cells in middle panels after the addition of 50 μM TPEN. Scale bars: 25 μm. (c) Confocal fluorescence images of exogenous Zn^{2+} uptake by hippocampal neurons upon glutamate (E) treatment. Hippocampal neurons were treated with 10 μM ZS5. The neurons were treated with 50 μM 1:2 Zn^{2+}/E and imaged in 1 min. The fluorescence enhancement upon Zn^{2+}/E treatment was marked by by asterisks. The fluorescence enhancement is removed after the following addition of 50 μM TPEN. Lysotracker Red was used as the red marker. Scale bar: 25 μm. (d) Time-lapse confocal fluorescent imaging of Zn^{2+} addition to primary cultures of hippocampal neurons pretreated with 10 μM ZS5. Top arrow stands for the addition of Zn^{2+}/pyrithione and the bottom arrow for the addition of TPEN. (e) Confocal fluorescence images of dentate gyrus neurons stimulated by nitrosative stress. The cells were treated with 10 μM ZS5 and SNOC in sequence. The fluorescence images were recorded at time points of 0, 1, 3, 5, and 7 min. The last image showed the fluorescence 2 min after addition of 200 μM TPEN. Scale bar: 25 μm. Adapted from ref. 77.

Single channel imaging of intracellular Zn^{2+} have been achieved using different turn-on Zn^{2+} fluorescent sensors.[78,79,80,81] LCSM imaging makes subcellular Zn^{2+} imaging especially in certain organelle more practical and promising. Although single channel Zn^{2+} imaging is becoming effective and practical due to the application of LCSM and visible light excitable Zn^{2+} sensors, this turn-on strategy only provides qualitative information on Zn^{2+}. Variable local sensor concentration, microenvironment and other imaging parameters often affect the observed fluorescence intensity.

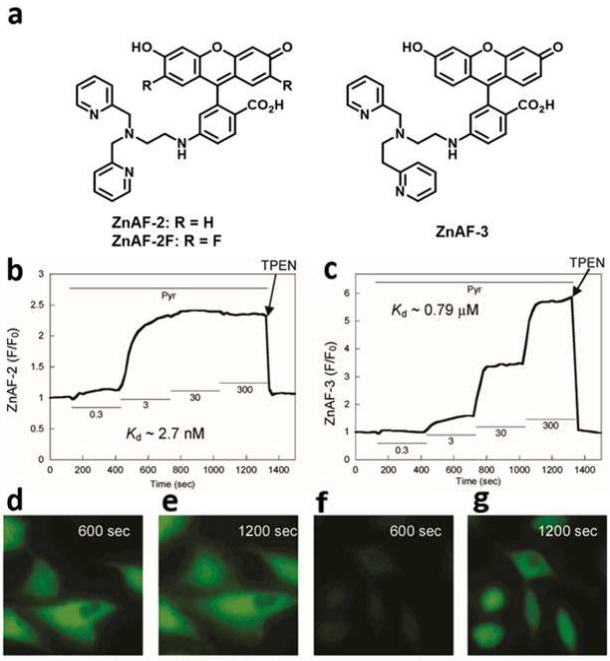

Fig. 9 (a) Chemical structures of ZnAF family sensors. Fluorescence response (b-g) of ZnAF-2DA in CHO cells incubated with (b) ZnAF-2 DA or (c) ZnAF-3 DA upon excitation at 470-490 nm was measured at 20 s intervals. Cells were exposed to pyrithione at 2 min and sequentially add increased concentrations of extracellular Zn^{2+} (0.3, 3, 30, and 300 μM, each for 5 min) as indicated by the solid lines. Arrow indicated the addition of TPEN (starting at arrow). (c-f) Fluorescence images of CHO cells incubated with (d,e) ZnAF-2 DA (d, 600 s; e, 1200 s) or (f, g) ZnAF-3 DA (f, 600 s; g, 1200 s). Adapted from ref. 71.

3.2 Ratiometric Zn^{2+} sensing: multichannel imaging

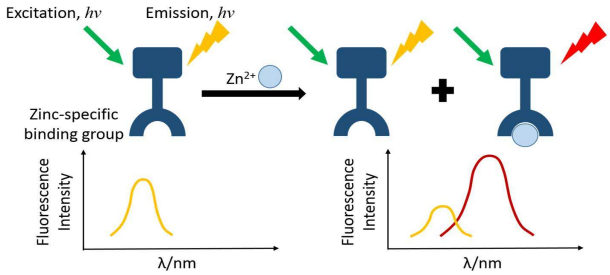

Fig. 10 Schematic diagram of the ratiometric Zn^{2+} detection using a ratiometric Zn^{2+} sensor.

To diminish the artificial interferences in the single channel turn on imaging induced by the deviated local sensor concentration, microenvironment and imaging factors, ratiometric fluorescence imaging based on multichannel mode have emerged and attracted more and more attentions. Different from single channel imaging mode, ratiometric fluorescent imaging normally measures analyte-induced change of the intensity ratio of two emission bands, which could eliminate most alteration in emission intensity induced by the above mentioned factors. This can be achieved by a self-calibration effect between two emission bands.

Disadvantages such as the photobleaching, autofluorescence can also be reduced. As shown in Fig. 10, Zn^{2+} binding to the sensor leads to a new emission band, and the intensity ratio between the two bands stands for the ratio of Zn^{2+} binding complex to apo sensor, and the artificial interference in fluorescence intensity can be reduced. If the ratiometric linear response range was determined, Zn^{2+} concentration can be quantified. Therefore, ratiometric Zn^{2+} imaging offers a powerful approach for quantitative imaging of biological Zn^{2+}, and even more powerful in the clarification of minor Zn^{2+} deviation.

Other ratiometric modes such as dual excitation with single emission, dual excitation/dual emission mode are also proposed for ratiometric sensing and imaging of Zn^{2+}. Zn^{2+}-induced excitation shift or both emission and excitation shift is also suitable for ratiomertic Zn^{2+} imaging. Currently, only the dual emission mode with single excitation is able to determine fluorescence from different channel simultaneously among these different ratiometric modes based on current imaging technique. Other modes may suffer from delayed detection of the second emission if Zn^{2+} fluctuation is faster than the switch between the two channels. Small molecular ratiometric fluorescent Zn^{2+} sensors are mainly designed based on internal charge transfer (ICT) mechanism.[68,82,83,84] In these sensors, Zn^{2+} coordinating atoms such as N or O are directly integrated as donor or acceptor of ICT fluorophore. Zn^{2+} binding changes the photo-induced ICT and results in a shift in emission or excitation.

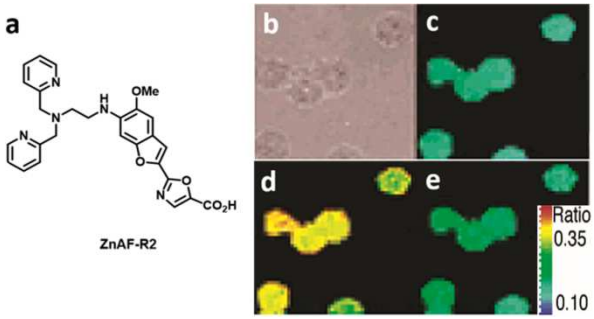

Fig. 11 Fluorescence ratiometric images (340 nm/380 nm) of Zn^{2+} in macrophages (RAW264.7) labeled with ZnAF-R2EE. (b) Bright-field transmission image; (c) ratiometric image of (b); (d) ratiometric image of cell in (c) upon Zn^{2+}/pyrithione incuabtion; (e) ratiometric image of cells in (d) was further treated by TPEN. Adapted from ref. 85.

The first ratiometric imaging for intracellular Zn^{2+} was reported by Nagano and coworkers in RAW 264.6 cells using a inverted fluorescence microscope, and the ratiometric Zn^{2+} sensor ZnAF-R2,[85] which displayed a specific Zn^{2+}-induced blue shift of excitation maximum. The dual excitation (340 and 380 nm) with single emission mode was conducted for this ratiometric imaging, and the ethyl ester derivative of this sensor, ZnAF-R2EE, was loaded into ZnAF-R2 as the imaging agent. The cytosolic esterase promoted the hydrolysis of the ester form of sensor, which trapped the final sensor anion within the cell. The imaging revealed that the ratio of fluorescence upon excitation at 340 nm to that upon excitation at 380 nm increased obviously in entire cells upon Zn^{2+} addition immediately (Fig. 11), the RLS imaging procedure confirmed the reversible ratiometric Zn^{2+} imaging ability of ZnAF-R2.

The ratiometric imaging for intracellular Zn^{2+} with LCSM was later reported by Lippard and co-workers using a ratiometric Zn^{2+} sensor based on a tautomeric seminaphthofluorescein, ZNP1.[86] This sensor displayed the specific Zn^{2+}-induced increase of emission ratio of fluorescence at 612 to that at 526 (I_{612}/I_{526}), therefore, a dual emission mode was adopted for the first time for the ratiometric Zn^{2+} imaging in live cells. Besides the RLS imaging procedure to confirmed the reversible ratiometric Zn^{2+} imaging ability, the RSS imaging procedure with SNOC as the stimulating agent has also been carried out, and the endogenous Zn^{2+} release from the metalloproteins induced by NO stimulation was monitored in a ratiometric manner for the first time, and the increased ratio upon SNOC incubation was distinctly decreased upon the followed TPEN treatment, which confirmed that the ratio increase is induced by the enhancement of labile Zn^{2+} level (Fig. 12).

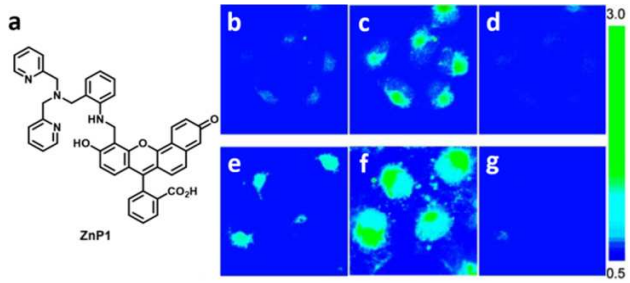

Fig. 12 Ratiometric Zn^{2+} imaging in COS-7 cells stained by ZNP1-Ac using LCSM. Fluorescence was collected in 10.7-nm optical windows centered respectively at 612 and 526 nm. λ_{ex}, 488 nm. Pseudocolor images depict the ratio of fluorescence intensities at these two windows. (b) Ratiometric image of cells incubated with 20 μM ZNP1-Ac; (c) image of the ZNP1-stained cells incubated with 50 μM $Zn(pyrithione)_2$; (d) image of cells in (c) was treated further with 100 μM TPEN. (e) Ratiometric image of the cells incubated with 20 μM ZNP1-Ac; (f) image of cells in (e) after incubated with 10 mM SNOC; (g) image of cells in (f) was incubated further with 2 mM TPEN. Adapted from ref. 86.

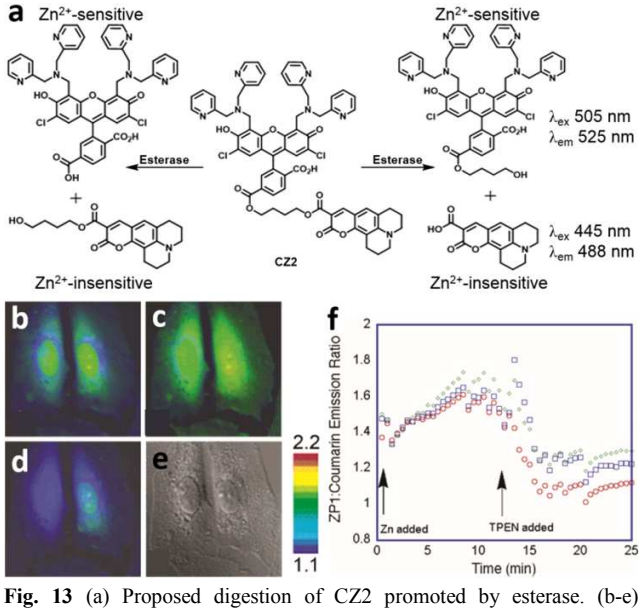

Fig. 13 (a) Proposed digestion of CZ2 promoted by esterase. (b-e) Fluorescence ratio images of HeLa cells treated with CZ2 after addition of Zn^{2+}/pyrithione (b, 0 min; c, 8 min), and the subsequent treatment with TPEN (d, 8 min). (e) The related DIC image of the cells. (f) Intensity ratios of $I_{ZP1}/I_{coumarin}$ as a function of time. Three separate regions of interest were defined at the start of the experiment and the ratio was

measured at 30 s intervals. Zn^{2+}/pyrithione (45 μM) were added at 5 min, and TPEN (50 μM) was added at 17 min. Adapted from ref. 87.

The ratiometric Zn^{2+} imaging with the dual excitation/dual emission mode has also been reported by Lippard and coworkers with ratiometric Zn^{2+} sensors CZ1 or CZ2, in which a coumarin fluorophore was integrated with a ZP1 moiety via an ester bond.[87,88] This sensor can be cleaved into two independent molecules, ZP1 and coumarin by intracellular esterase after loaded into the cells. Thereafter, exciting at 400-440 nm led to the coumarin emission around 475 nm which is stable even in the presence of Zn^{2+}, and coumarin is able to act as the reference. Excitating at 460-500 nm displayed the ZP1 emission, which is enhanced upon Zn^{2+} binding, and the ratio of the fluorescence intensities $I_{ZP1}/I_{Coumarin}$ shows the specific increment upon Zn^{2+} binding. The dual excitation/dual emission mode imaging via the RLS procedure showed that the ratiometric imaging ability of this sensor is reversible in HeLa cells (Fig. 13), and the the dual excitation/dual emission imaging mode is effective for intracellular Zn^{2+} fluctuation induced by Zn^{2+}/pyrithione incubation and the following TPEN treatment.

Ratiometric Zn^{2+} imaging can also been realized using FP-based macromolecule ratiometric Zn^{2+} sensors based on FRET mechanism,[89,90,91,92] where resonance energy transfer from a donor fluorophore to an acceptor fluorophore occurs via a non-radiative "dipole–dipole" coupling.[93,94] The emission spectrum of donor fluorophore overlaps with the absorption spectrum of acceptor fluorophore. The FRET efficiency between the two fluorophores is determined by the overlap, donor-acceptor distance and orientation of the donor and fluorophore dipoles. Zn^{2+}-induced alteration of the three factors changes the FRET efficiency, which enables ratiometric Zn^{2+} imaging by detecting simultaneously the emission of donor and acceptor.[93,94] The linkers between the two FPs are normally specific Zn^{2+} affinity peptides or proteins such as zinc fingers.

A number of FP-based ratiometric Zn^{2+} sensors have been designed and successfully applied to ratiometric monitoring of intracellular Zn^{2+} homeostasis. In Zif- and Zap-based FRET Zn^{2+} sensors, zinc finger domain was adopted as Zn^{2+} chelator.[89,91] The subcellular application of the sensors in Zn^{2+} imaging will be introduced in Section 5. Intracellular Zn^{2+} quantification has been realized using a series of genetically encoded FRET-based ratiometric Zn^{2+} sensors.[90, 95,96] In these sensors, Atox1 and the fourth domain of ATP7B (WD4) were integrated as Zn^{2+}-binding motif, each domain providing two cysteine residues to form a single tetrahedral zinc binding pocket (Fig. 14a). With Cerulean and Citrine as FRET donor and acceptor, eCALWY family sensors were developed with different Zn^{2+} affinity.[92] In addition, mutations (S208F and V224L) were introduced on the surface of both fluorescent domains to promote intramolecular complex formation, which considerably improved the ratiometric response. Distance between the two FPs was increased upon Zn^{2+} binding, leading to the decreased FRET efficiency and the emission raito change. When the ratiometric Zn^{2+} imaging with these similar sensors of different Zn^{2+} affinity was determined, the sensor occupancy can be calculated based on the emission ratio of sensor expressed in INS-1(832/13) cells after treating with TPEN and Zn^{2+}/pyrithione. Then, the sensor occupancies as a function of individual K_d of these sensors were plotted. A non-linear least-squares fit of the data points gave a sigmoidal shape that is consistent with a free Zn^{2+} concentration of ~ 0.4 nM (Fig. 14e). Similar results were obtained in HEK293 cells. Substantially higher Zn^{2+} concentration was found in insulin containing secretory vesicles. This is an elegant example showing intracellular Zn^{2+} quantification can be achieved using sensors of different Zn^{2+} affinity without knowing the local sensor concentration.

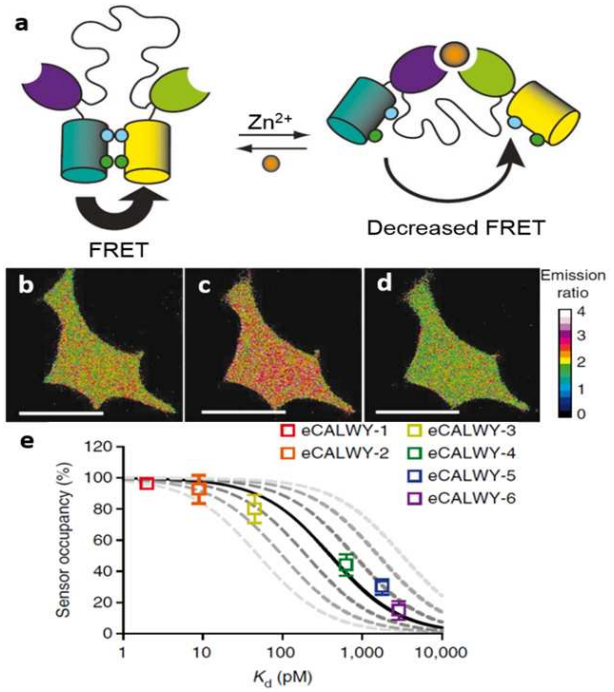

Fig. 14 (a) Schematic diagram of the Zn^{2+} sensing mechanism of eCALWY sensor. Atox1 and the fourth domain of ATP7B (WD4) were used as Zn^{2+}-binding domains. (b-d) False-colored spinning disc confocal microscopy images of INS-1(832/13) cells expressing eCALWY-4 after perifusion with KHB (b), KHB with 50 μM TPEN (c) and KHB with 5 μM pyrithione and 100 μM Zn^{2+} (d). Scale bar, 15 μm. (f) Sensor occupancy in pancreatic β-cells (INS-1(832/13)) as a function of the sensor K_d. Data points show the occupancy of the different eCALWY variants under resting conditions. The dashed lines depict the expected responses assuming free zinc concentrations of 0.05, 0.1, 0.2 (0.4, solid line), 0.8, 1.6, and 3.2 nM, respectively. Adapted from ref. 92.

Ratiometric sensing mode renders zinc imaging the quantitative capacity, and the rational design of ratiometric Zn^{2+} sensors is essential. Beside the above mentioned mechanisms to design ratiometric sensors for Zn^{2+}, the excited-state intramolecular proton transfer (ESIPT) has also been frequently adopted to design ratiometric Zn^{2+} sensors.[97,98,99] Several other approaches on the design of ratiometric sensors have been adopted and summarized in recent reviews.[100,101,102]

3.3 Intracellular TP and NIR fluorescence Zn^{2+} imaging

Photo-excitation at short wavelength, especially UV excitation, leads to promoted generation of free radicals and reactive oxygen species (ROS), which cause photodamage, photo-bleaching and shortened tracking time. Endogenous fluorophores (e.g. aromatic amino acids, NADH, flavone, etc.) can be excited at short wavelengths (< 450 nm),[103, 104] which induces not only autofluorescence interference but also higher tissue scattering and absorption to limit imaging depth.

NIR sensors have emission or excitation maxima (650-900 nm, NIR I) in the NIR region, which provides advantages in fluorescence imaging, since NIR photons cause minimum photo-induced damage to biological samples. NIR photons reduce photobleaching and favour long term tracking. NIR imaging provides better S/N ratio due to reduced autofluorescence in biological specimens. More importantly, NIR shows less light scattering and absorption in tissue and offers higher imaging depth, which makes NIR sensors more favourable for *in vivo* imaging (Fig.15).[105] Therefore, developing NIR sensors is an effective way to improve imaging quality and prolong effective imaging time, especially for *in vivo* imaging.[106,107]

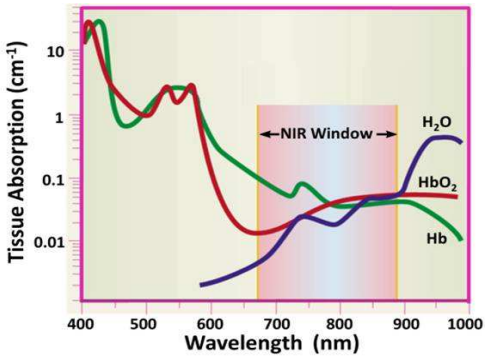

Fig. 15 NIR window is suited for *in vivo* imaging because of minimal light absorption by hemoglobin(<650 nm) and water (>900 nm). Adapted from ref. 105.

The first NIR sensor for Zn^{2+} was constructed by integration of a NIR fluorophore tricarbocyanine and a Zn^{2+} chelator dipicolylethylenediamine,[108] but first NIR intracellular Zn^{2+} imaging was realized in live macrophage cells using another Zn^{2+} sensor, DPA-Cy, shortly afterwards.[109] This sensor showed a λ_{em} at 800 nm with a 20-fold enhancement in response to Zn^{2+} upon excitation at 731 nm. The successful NIR imaging via RLS procedure confirmed its cell permeability and rapid reversible zinc imaging ability (Fig. 16). As shown in Fig.16, background autofluorescence in NIR imaging for intracellular Zn^{2+} is almost negligible compared to the case shown in Fig. 7.

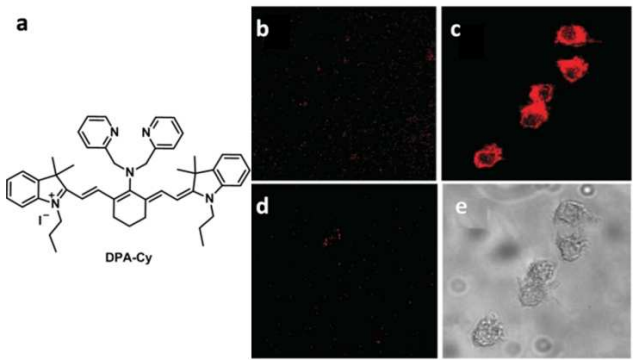

Fig. 16 (a) Chemical structure of DPA-Cy. Confocal fluorescence images of live macrophage cells stained with 5 μM DPA-Cy in the absence (b) and presence (c) of 100 μM Zn^{2+}; (d) fluorescent image of cells in (c) after TPEN treatment; (e) bright field image. Adapted from ref. 109.

As one of the most commonly used NIR fluorophores, cyanines exhibit large extinction coefficient and moderate quantum yield, but cyanine sensors often suffer from poor photostability. Therefore, other NIR fluorophores such as BODIPY derivatives,[110] phenoxazinium skeleton[111] and silicon-substituted rhodamine (Si-rhodamine)[112] were adopted for NIR Zn^{2+} imaging. For example, Si-rhodamines have emerged as a new NIR fluorophore which shows high quantum yield, large absorption and high tolerance to photobleaching.[113,114]

Two-photo microscopy (TPM), a variant of the multiphoton microscopy (MPM), was pioneered by Denk and Webb in 1990.[115] In TPM, a fluorophore is excited by absorbing simultaneously two photons with lower energy (in NIR range) and falls back to the ground state by emitting one photon (Fig. 17).[116,117] Therefore, the emission wavelength of a two-photon absorption (TPA) fluorophore is shorter than the excitation wavelength, which leads to an inverse Stokes shift. Since the statistical probability of a fluorophore absorbing two photons simultaneously is quite low, a pulsed laser (normally a femtosecond laser) with high power is required as the light source in order to produce high flux of excitation photons for two photon excited fluorescence (TPEF). The TP excitation normally merges into NIR range, therefore, TPM also takes the advantages of NIR imaging.

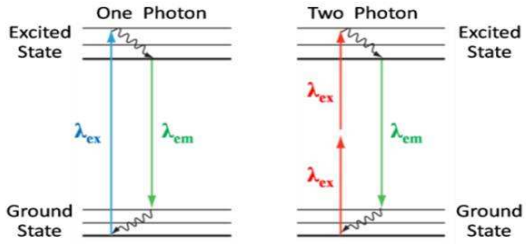

Fig. 17 Simplified Jablonski diagrams for one-photon (left) and two-photon (right) fluorescence. Adapted from ref. 116.

Recently, TPM has gained much interest in biological imaging for biological species in tissues and small animal models.[118,119] As TPEF is emitted only at the focal point, TPM provides not only high spatial resolution but also function of optical sectioning with no pinhole requirement. The optical sectioning is helpful for the construction of 3D image by imaging hundreds of x−y planes along the *z* direction of a live tissue. As to TP imaging for Zn^{2+}, Zn^{2+} sensors should have a large TP cross section (δ_{TPA}) and high fluorescent quantum yield (Φ) to yield a large TP action cross section ($\Phi\delta_{TPA}$), which can be viewed as the brightness of the TPEF. In general, a TP sensor with a $\Phi\delta_{TPA}$ value over 50 GM is preferred for TP imaging.

The first TP Zn^{2+} imaging was reported by O'Halloran et al. with Zn^{2+} sensor Zinbo-5.[120] Zinbo-5 exhibited a red emission shift from 407 to 443 nm upon Zn^{2+} binding, with a zinc affinity pZn of 9.3. Although the TP cross section data was not provided, the related TP ratiometric imaging of Zn^{2+} in fixed mouse fibroblast cells was demonstrated upon excitation at 710 nm with emission channels set in a 10.7 nm windows centered at 445 and 402 nm respectively (Fig.18). The RLS imaging procedure clearly showed a reversible ratiometric imaging ability for Zn^{2+}. Using Zinbo-5 as the imaging agent, O'Halloran et al. found a 4-fold higher Zn^{2+} concentration in the parasite-infected cells than that of the uninfected ones, suggesting that the massive zinc fluxes are essential for an intracellular eukaryotic parasite during the infection cycle.[121] The intracellular TP ratiometric Zn^{2+}

imaging using a 6-substituted quinolone-based Zn^{2+} sensor was also reported.[122]

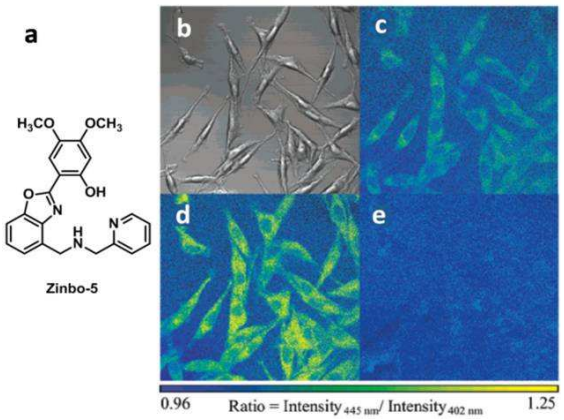

Fig. 18 (a) Chemical structure of Zinbo-5. (b-e) TP fluorescence ratio images of fixed fibroblast [L(TK)$^-$] cells stained with Zinbo-5. (b) Bright field image; (c) emission ratio image in the absence of Zn^{2+}; (d) emission ratio image of cells in (c) was further treated by Zn^{2+}/pyrithione; (e) emission ratio image of the cells in (d) after treatment with TPEN incubation. Adapted from ref. 120.

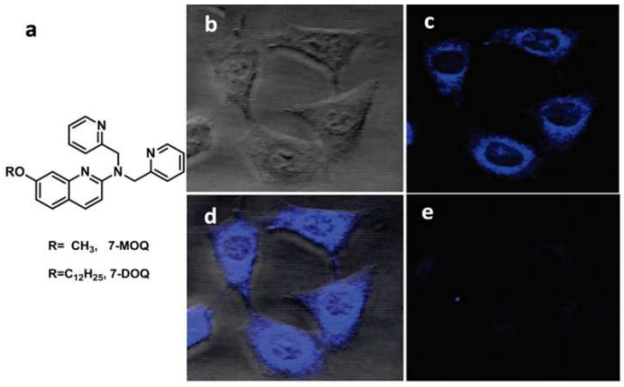

Fig. 19 (a) Chemical structure of 7-MOQ and 7-DOQ. (b-e): TPF images of living A431 cells labelled with 30 μM 7-DOQ. (b) Bright field image of the cells; (c) TP fluorescence image of the cells after treatment with Zn^{2+}/pyrithione; (d) Overlay of (b) and (c); (e) TP fluorescence image of the cells in (c) treated further by TPEN incubation. Adapted from ref. 123.

Intracellular TP turn-on Zn^{2+} imaging was achieved using a 7-hydroxyquinoline based TP sensor (7-MOQ).[123] A cell permeable dodecyloxy derivative 7-DOQ was also used for turn-on Zn^{2+} imaging in TP confocal microscopy. Upon excitation at 800 nm, the TPEF intensity of A431 cells labelled with 7-DOQ increased after the addition of 1:1 zinc(II)/pyrithione and decreased upon treatment with TPEN (RLS procedure, Fig. 19), confirming its reversible imaging ability.

The most attractive property of NIR and TP imaging is their suitability for biological imaging in tissues, organs and living animal models due to their deeper optical tissue penetration, which will be discussed in details in Section 6.

4. Lifetime-based intracellular Zn^{2+} imaging

Another practical approach for eliminate autofluorescence in biological samples is photoluminescence lifetime based imaging. The luminescence lifetime τ refers to the average time a fluorophore remains in the excited state after excitation, and normally defined as the time required by a population of excited molecules to decrease exponentially to N/e via the loss of energy through luminescence and other non-radiative processes.[124] Typically, luminescence lifetime is an intrinsic property of a luminophore which will not be affected by factors such as sensor concentration, excitation, photobleaching and detection condition. However, luminescence lifetime can be sensitive to either internal molecular vibrations and rotations or external factors such as the transfer of the excitation energy to other molecules or environment through FRET, Dexter electron transfer and dynamic quenching.[125] Thus, imaging of luminescence lifetime can be used to probe the surroundings of a fluorophore and be able to distinguish molecules with similar luminescence spectra but different lifetime.[126]

Different from intensity based imaging, FLIM clearly resolves sensor location based on lifetimes.[127] As illustrated in Fig. 20, the different environments in regions 1 and 2 will not be detected by the intensity-based imaging while FLIM will reveal the distinct environments of regions 1 and 2 based on the detected lifetimes. Moreover, due to its independence of sensor concentration, lifetime based imaging may act as a complementary method of ratiometric imaging, providing quantitative information of interested analytes such as Zn^{2+} according to analyte-induced lifetime alteration.[128,129,130]

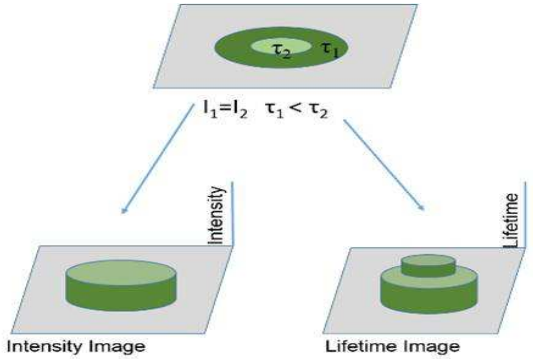

Fig. 20 Intuitive presentation of the concept of FLIM. Assume that the two regions in the object display the same fluorescence intensity but different decay times, $\tau_2 > \tau_1$. Adapted from ref. 124.

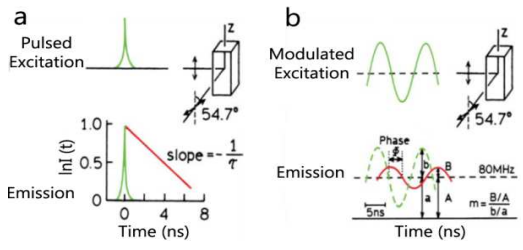

Fig. 21 Time-domain (a) and frequency-domain (b) of lifetime-based measurements. Adapted from ref. 124.

As a time-resolved image acquisition method, FLIM can provide time-resolved information by time-domain or frequency-domain data acquisition methods (Fig. 21).[131,132] In time-domain, the sample is excited with a short optical pulse and then the decay of the fluorescence intensity is detected through time-correlated single photon counting (TCSPC) gating or a streak camera. For frequency-domain technique, the decay time is obtained from fluorescence demodulation and phase shift calculation after

exciting the sample with periodically modulated excitation beams.[124] These approaches to FLIM are mathematically equivalent and their data can be interconverted through Fourier transform. In both methods, the lifetime is calculated using curve fitting algorithms.[125]

Lifetime imaging depends on sensor lifetime change in response to the change of sensor structure or sensor surrounding. Quin-2,[133,134] calcium crimson,[135] Calcium Green and Fluo-3[136] have been successfully applied for intracellular imaging of Ca^{2+} using FLIM. In these cases, FLIM has been proved to be more reliable than intensity-based imaging methods especially in eliminating the interference of autofluorescence. However, the fluorescence lifetime-based fluorescent Zn^{2+} sensors are rare compared to intensity-based Zn^{2+} sensors. Small organic dyes usually have fluorescence lifetime of nanoseconds or sub-nanoseconds, and it is difficult to develop small organic fluorescent sensors with big lifetime change that is essential for FLIM. Commercial available Newport Green DCF exhibited an over 3-fold elongation of lifetime upon Zn^{2+} addition, from 0.88 to 2.93 ns, which resulted in the phase angle change of 27° at 60 MHz modulation frequency.[131] This property can be used to quantitate or image Zn^{2+} levels or fluxes. Fluorescence lifetime Zn^{2+} imaging with Newport Green DCF was carried out in CA1 pyramidal cells of rabbit brain to quantify the labile Zn^{2+} level after being killed by excitotoxic Zn^{2+} release due to transient global ischemia. In this experiment, complete microscopic frequency scan on small region of interest was carried out and the phases and modulation were fitted with the decay law and the concentration of labile Zn^{2+} can be derived. Moreover, the Zn^{2+} level can be calibrated readily with frequency scan on cuvette containing Zn^{2+} of different levels. With this advantage, the complete frequency scan (or decay curve, in the time domain) displayed additional advantage over phase or modulation measurements at a single frequency. Therefore, FLIM is another reliable approache to acquire the quantitative information of Zn^{2+} in living systems.

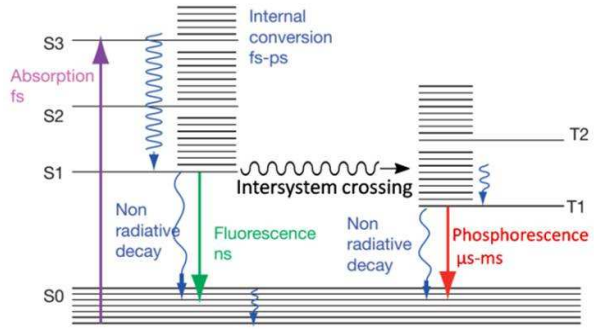

Fig. 22 Jablonski diagram and time scale of photophysical processes for organic molecules. Adapted from Ref. 125.

Phosphorescence is a radioactive decay from T_1 to S_0 after the intersystem crossing (ISC) from excited state S_1 to T_1, which shows much longer emission lifetime than fluorescence (Fig. 22).[125] Most luminescent transition and lanthanide metal complexes emit with a phosphorescence mechanism. Since endogenous fluorophores display fluorescence lifetimes shorter than 100 ns, imaging with long-lived phosphorescence sensors can eliminate the interference of autofluorescence by time-gated measurements. Luminescent metal complexes usually offer tuneable colour, large Stokes shift as well as fine aqueous solubility. These complexes are mainly classified into two categories: luminescent 2nd/3rd-row transition metal complexes formed by the conjugated organic ligands (Os^{2+}, Re^{3+}, Ru^{2+}, Ir^{3+} and Pt^{2+}) in which the luminescence was orginated from MLCT and d-d transitions; and lanthanide complexes (Ln^{3+} complex, Ln^{3+} = Sm, Eu, Tb, Dy, Yb), whose emission arises from the LMCT and f-f transitions.[137]

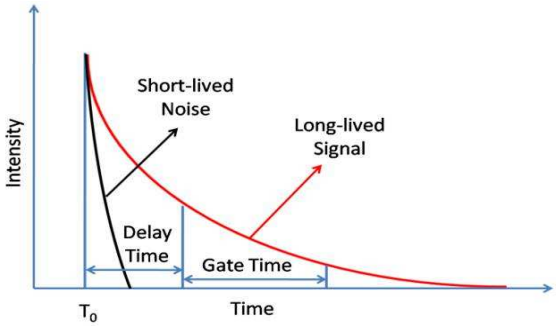

Fig. 23 Illustration of the principle of time-resolved long-lived luminescence microscopy (TRLLM). The short-lived background noise fluorescence (dark line) decays to negligible levels after an appropriate delay time, left only the long-lived luminescence (red line) which is collected in the gate time. Adapted from ref. 138.

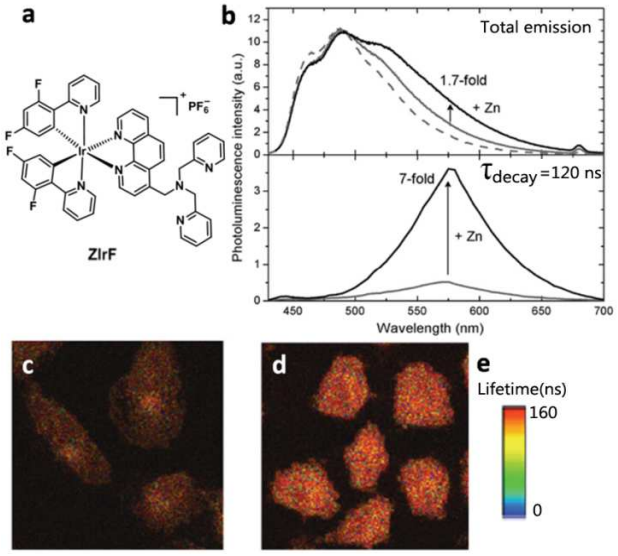

Fig. 24 (a) Chemical structure of **ZIrF**. (b) Time-gated acquisition of zinc-induced turn-on photoluminescence of **ZIrF**. Upper panel: total photoluminescence spectrum of an air equilibrated pH 7.0 buffer solution (25 mM PIPES) containing **ZIrF** (10 µM) and Acr^+ (2 µM). Solid gray line, total photoluminescence spectrum; dashed gray line, fluorescence spectrum of Acr^+ (2 µM); solid black line, spectrum after the addition of $ZnCl_2$ (5 equiv). Lower panel: Time-gated photoluminescence spectrum acquired after 120 ns delay. Gray line, zinc free state; black line, after $ZnCl_2$ (5 equiv) addition. (c and d) Fluorescence lifetime microscopic images (80 µm) of the fixed A549 cells stained with **ZIrF** in the absence (c) and presence (d) of exogenous Zn^{2+}. (e) Lifetime bar. Adapted from ref. 139.

Besides FLIM, time-resolved long-lived luminescence microscopy (TRLLM) also offers distinct advantages over intensity-based imaging. As shown in Fig. 23, interference of the short-lived background noise can be eliminated.[138] Nam and

Lippard reported the first phosphorescent Zn^{2+} imaging in biological samples.[139] A cyclometalating Ir(III) complex **ZIrF** displays a specific sensing ability for Zn^{2+}. The photoluminescence of **ZIrF** and 10-methylacridinium (Acr^+) exhibits only a small turn-on response (~1.7 fold) to Zn^{2+}, however, time-gated fluorescence spectrum acquired with a 120 ns delay displayed a 7-fold turn-on response to Zn^{2+}, where low lifetime fluorescence contribution from Acr^+ was removed (Fig. 24b). Intracellular Zn^{2+} imaging by phosphorescent sensor via FLIM was carried out in fixed A549 cells stained with **ZIrF**. An inverse time-resolved microscope upon excitation with a 375 nm picosecond pulsed diode laser at repetition rate of 2.5 MHz was used. The lifetimes obtained for the midrange (τ_2) and short-lived (τ_3) components are invariant upon Zn^{2+} loading into the cells, while for the long-lived component, average photoluminescence lifetime (τ_1) was increased from 120 to 130 ns (Fig 24c-e).

A similar Ir(III) based sensor **ZIrdCF$_3$** was applied for lifetime-based imaging of intracellular Zn^{2+} in HeLa cells.[140] Free **ZIrdCF$_3$** showed a lifetime of 0.0512 ns, whereas its Zn^{2+} bound form exhibited a significantly longer lifetime of 5.35 μs. A lifetime-based imaging of fixed HeLa cells incubated with **ZIrdCF$_3$** showed significant increase of lifetime in the present of Zn^{2+} (Fig. 25). These studies provided useful guidelines for the future design of phosphorescence sensor for lifetime Zn^{2+} imaging.

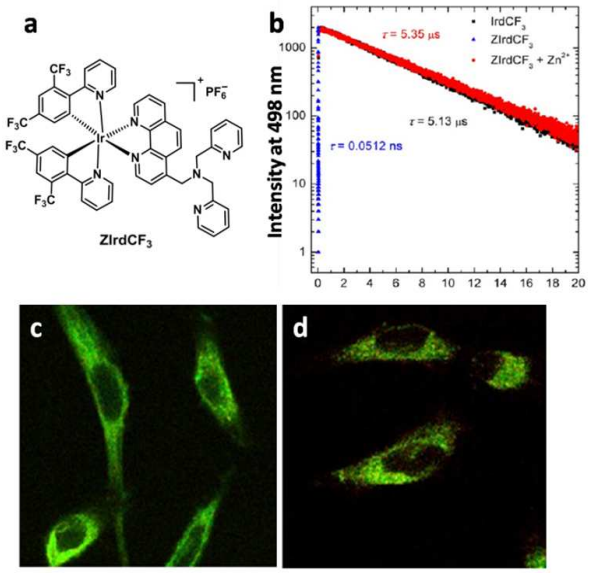

Fig. 25 (a) Chemical structure of **ZIrdCF$_3$**. (b) Phosphorescence decay profiles of **ZIrdCF$_3$** in the absence (blue) and presence (red) of Zn^{2+}. (c, d) FLIM images (80 μm × 80 μm) of the fixed A549 cells stained with **ZIrdCF$_3$** in the absence (c) and presence (d) of exogenous Zn^{2+}. Adapted from ref. 140.

A lanthanide based complex [**Eu-7**] was developed by Nagano and co-workers for TRLLM imaging of Zn^{2+}.[141] Beside turn-on response to Zn^{2+}, the luminescence lifetime of [**Eu-7**] in the presence of Zn^{2+} was also elongated from 0.52 ms to 0.58 ms, suggesting that [**Eu-7**] was able to minimize the short-lived autofluorescence in cells and provide a high S/N ratio. The TRLLM imaging of [**Eu-7**] in living HeLa cells showed a significant increase of luminescence induced by Zn^{2+}/pyrithione incubation. The intracellular Zn^{2+} alteration upon 15 min of extracellular TPEN incubation could be monitored clearly (Fig. 26). Since long-lived phosphorescence signal of [**Eu-7**] displays longer lifetime than the co-staining dye rhodamine 6G, TRLLM Zn^{2+} imaging using [**Eu-7**] proved the advantage of lifetime imaging techniques.

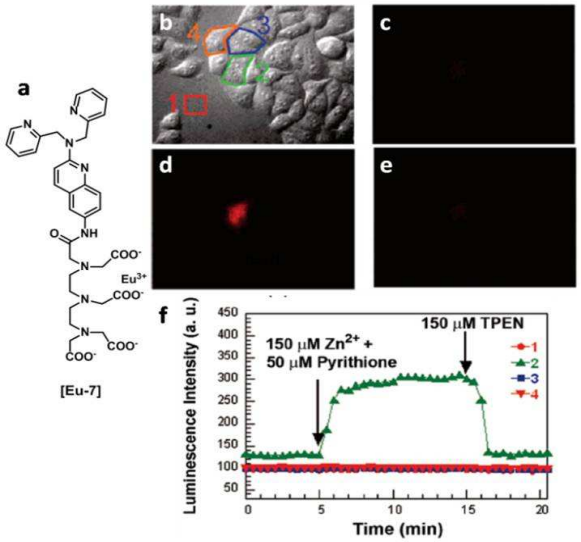

Fig. 26 (a) Chemical structure of complex [**Eu-7**]. (b-d) Time-resolved long-lived luminescence imaging of intracellular Zn^{2+} in living HeLa cells. (b) Bright-field transmission image (0 min). (c) Time-resolved long-lived luminescence image of (b) (0 min). (d) Time-resolved long-lived luminescence image (7 min) following addition of Zn^{2+} at 5 min. (e) Time-resolved long-lived luminescence image (17 min) following addition of 100 μM TPEN to the medium at 15 min. (f) The average intensity of the corresponding area of cell area in (b). 1, Extracellular region; 2, intracellular region of the injected cell; 3, 4, intracellular regions of noninjected cells. Adapted from ref. 141.

Similar intracellular TRLLM Zn^{2+} imaging was realized using a terbium (Tb^{3+}) chelate-based luminescent chemosensor, **BBATA-Tb^{3+}**.[142] The weak luminescence of **BBATA-Tb^{3+}** can be selectively and significantly enhanced (6.0-fold) upon Zn^{2+} binding. The autofluorescence from the cells could be completely suppressed by TRLLM using a time-resolved digital black-and-white CCD camera system with the selected delay time, gate time, lamp pulse width and exposure time settings.

5. Subcellular Zn^{2+} imaging

Mammalian cells are the most commonly used biological specimens for intracellular Zn^{2+} imaging, which contains many subcellular compartments such as mitochondria, lysosome, Golgi apparatus, endoplasmic reticulum (ER), etc. These subcellular compartments play different roles in intracellular Zn^{2+} homeostasis. Labile Zn^{2+} concentrations in these subcellular apparatuses vary from one to another.[143] It was reported that labile Zn^{2+} level in ER and Golgi apparatus of HeLa cells was in the range of ~ 1 pM, those in cytosol and nucleus were about two-order of magnitude higher whereas in mitochondria was 10-fold lower.[100] Moreover, labile Zn^{2+} level in the same organelle is variable with the cells lines, cell phases, and physiological processes. Therefore, it is highly appealing to visualize labile Zn^{2+} within specific subcellular compartments for the study of inter- and intra-organelle Zn^{2+} physiology. Considerable efforts

have been devoted to this subject during the past few years.

All cell permeable Zn^{2+} sensors have their own specific intracellular distribution patterns, although most of which have not been fully explored so far. From the reported imaging results, most of available Zn^{2+} sensors seem to be distributed almost uniformly in the cytosol, yet a few Zn^{2+} sensors showed punctuated, rodlike, or filamentous bright signals inside the cell, indicating a preferential affinity of sensor to certain organelles.

The subcellular localization of a tested sensor can be evaluated by co-staining experiment with commercially available fluorescent markers with known specific subcellular localization pattern but has no emission (or excitation) overlap with tested sensors. Co-localization parameters, such as Pearson's correction coefficient which is given by imaging software, are used to quantify the degree of co-localization between sensor and organelle marker. [144] For co-localization imaging, confocal microscopy is preferable due to its high spatial resolution.

Three major strategies have been adopted to construct Zn^{2+} sensors for specific subcellular compartment: 1) small molecular sensors modified with a specific targeting group for certain organelle; 2) genetic-encoded sensors which can be selectively expressed in a particular organelle; 3) genetic-synthetic hybrid sensors.

5.1 Mitochondrial Zn^{2+} imaging

Mitochondria are primary subcellular compartment in eukaryotic cells for energy-generating, which play vital roles in various physiological processes including proliferation and apoptosis. [145, 146] Many Zn^{2+}-dependent enzymes are located in mitochondria, and Zn^{2+} pools are essential for maintaining mitochondrial protein functions. [147,148] Most ROS/RNS in living systems are generated in mitochondria during the production of ATP, which mobilize mitochondrial Zn^{2+}. [149] Mitochondria have a slightly basic pH value of ~ 8.0 with a negative cross membrane potential (ca. -180 mV, outer to inner). In general, fluorescent sensors with a lipophilic cationic nature tend to accumulate in mitochondria driven by the cross inner membrane potential of mitochondria. [150]

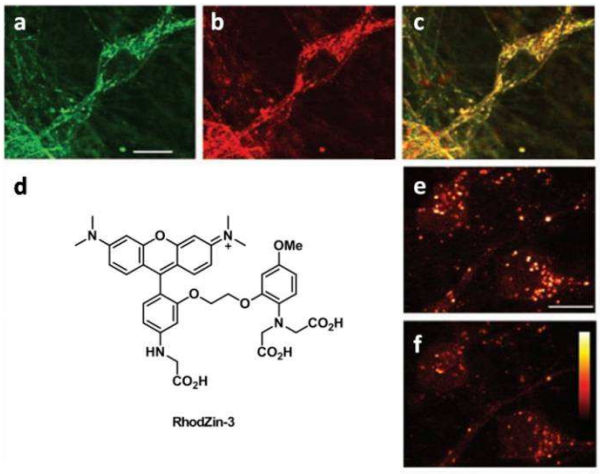

Fig. 27 Co-localization study of MitoTracker Green (green fluorescence, a) and RhodZin-3 (red fluorescence, b) in cortical neurons via confocal fluorescence microscopy showed the fine overlay between the two dyes (c). (d) Chemical structure of RhodZin-3. Confocal fluorescence image of neurons stained with RhodZin-3 before (e) and after (f) treatment with TPEN. Scale bars, 20 μm. Adapted from ref.151.

The first mitochondrial Zn^{2+} imaging was reported by Weiss and co-workers in 2003 using a Zn^{2+} sensor rhodZin-3 (AM), which exhibited a 75-fold fluorescence enhancement upon Zn^{2+} binding with a dissociation constant of 65 nM. [149, 151] Due to the lipophilic cationic nature, rhodamine-based sensors tend to accumulate in mitochondria. [152] Colocalization study showed a substantial overlap between RhodZin-3 and MitoTracker Green in the cultured cortical neurons (Fig. 27). Mitochondrial Zn^{2+} pool was confirmed, which is distinct from the cytosolic protein or ligand-bound pools for Zn^{2+}.

Triphenylphosphonium (TPP), another lipophilic cationic group, is one of the most commonly used targeting group for mitochondria. [153] Turn-on imaging for mitochondrial Zn^{2+} with TPP-bearing sensor has been realized by Lippard and coworkers with a Zn^{2+} sensor DA-ZP1-TPP in mitochondria of healthy and cancerous prostate cells. [154] Tumorigenic cells, in contrast to healthy epithelial prostate cells, were found unable to accumulate mobile zinc within their mitochondria.

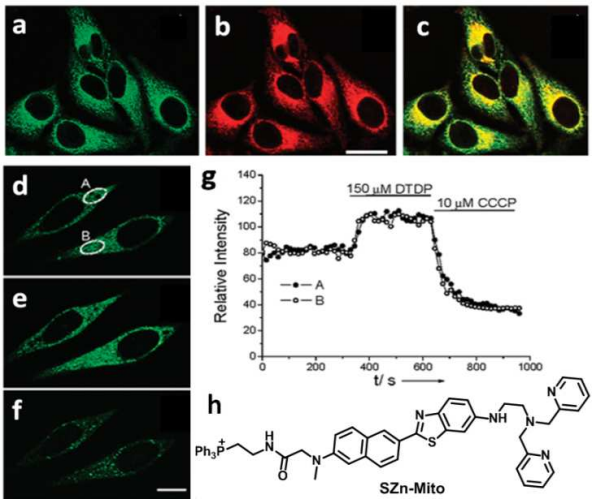

Fig. 28 TPM (a, for TPEF of SZn-Mito) and SPM (b, for SPF of MitoTracker Red FM) images of HeLa cells co-stained by SZn-Mito (0.5 μM) and MitoTracker Red FM (1 μM) for 30 min. (c) Overlay image of (a) and (b). The excitation wavelengths for TPEF and SPF were 760 and 514 nm, respectively, and the emissions were collected at 450-550 (SZn-Mito) and 600-700 nm (Mitotracker Red FM). Scale bar in (b), 20 μm. (d-f): TPM images of SZn-Mito-stained HeLa cells before (d) and after (e) DTDP (150 μM) addition and the followed CCCP (10 μM) addition (f). Scale bar in (f), 20 μm. (g) Temporal profiles of the TPEF intensity in ROIs (A) and (B) in (d) determined during DTDP and CCCP treatment. (h) Chemical structure of SZn-Mito. Adapted from ref. 155.

Sensors containing TPP group such as SZn_Mito, SZn2-Mito, and FZn-Mito have been tested for TPM turn-on Zn^{2+} imaging in mitochondria. [155, 156] SZn-Mito showed a 7-fold TPEF enhancement in response to Zn^{2+} with a dissociation constant (K_d^{TP}) of 3.1 nM. SZn2-Mito exhibited a 70-fold TPEF enhancement in response to Zn^{2+} with a K_d^{TP} of 1.4 nM. The TPEF intensity of FZn-Mito increased by 16-fold upon Zn^{2+} addition and the related K_d^{TP} was determined to be 17 nM. These sensors were found to localize in mitochondria with Pearson's correction coefficients ranging from 0.85 to 0.89 (Fig. 28). In addition, labile Zn^{2+} fluctuation in mitochondria of HeLa cells

triggered by DTDP (a reagent that promotes Zn^{2+} release from Zn^{2+}-binding proteins) and CCCP (a compound that promotes the release of intramitochondrial cations by collapsing the mitochondrial membrane potential) were monitored.

Ratiometric imaging for mitochondrial Zn^{2+} was realized with sensors bearing TPP group. It was firstly realized using a mitochondria targetable ratiometric Zn^{2+} sensor, DQZn2, which was constructed by integrating a TPP group with a quinoline-derived fluorophore.[157] Co-localization study with MitoTracker Deep Red showed a Pearson's correction coefficient of 0.86, confirming the mitochondria targeting ability of the sensor. Due to the high Zn^{2+} affinity (K_d, 0.45 nM), DQZn2 has been used in the ratiometric imaging of mitochondrial Zn^{2+} release upon S-nitrosocystein (SNOC) stimulation in a dual emission mode. A FRET based sensor tethered with a TPP group has also been developed for ratiometric imaging of mitochondrial Zn^{2+} via integrating a diamino-substituted naphthalenediimide with 5-(4-methoxystyryl)-50-methyl-2,20-bipyridine.[158]

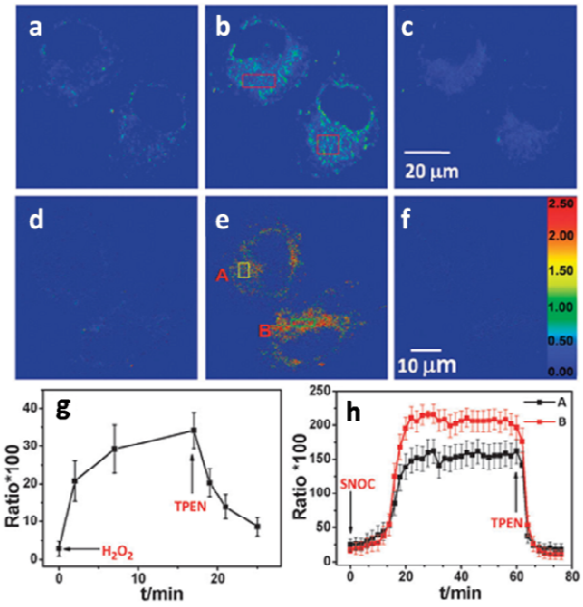

Fig. 29 Confocal fluorescence dual excitation ratiometric imaging of mitochondrial Zn^{2+} release in Mito-ST-stained MCF-7 cells. (a-c) Ratiometric images of the stained MCF-7 cells before (a) and after (b) H_2O_2 stimulation, followed by treatment with TPEN (c). (d-f) Ratiometric images of the stained cells before (d) and after (e) exposed to SNOC, followed by treatment with TPEN (f). (g, h) The related time profiles of emission ratio change in ROIs of Mito-ST-labeled MCF-7 cells (g, H_2O_2; h, SNOC). Adapted from ref. 159.

Dual excitation ratiometric imaging for mitochondrial Zn^{2+} has also been reported with Zn^{2+} sensor Mito-ST bearing also a TPP motif.[159] Mito-ST displayed a Zn^{2+}-induced excitation shift from 466 to 397 nm with a K_d of 8.2±0.2 nM for Zn^{2+}. High Pearson's correction coefficient of 0.95 between Mito-ST and MitoTracker in MCF-7 cells was observed, indicating an excellent mitochondria-targeting ability (Fig. 29). Dual excitation imaging at 405 and 488 nm disclosed a reversible ratiometric sensing ability for mitochondrial Zn^{2+}. Mitochondrial Zn^{2+} release upon H_2O_2 and SNOC stimulations was also monitored, suggesting a possible ''zinc pool'' in mitochondria. The advantage of ratiometric imaging over turn-on one is clearly demonstrated by H_2O_2-induced mitochondrial Zn^{2+} release.[160]

Cyanine group is another commonly used lipophilic cationic structure with mitochondria targeting ability, and sensors derived from cyanine have been successfully applied for the biological imaging in mitochondria.[161,162] However, cyanine-derived Zn^{2+} sensors with defined mitochondria-targeting ability have not been reported, although tricarbocyanine based Zn^{2+} sensors such as DPA-CY have been developed.

The accumulation of lipophilic cation based Zn^{2+} sensors in mitochondria is dependent on the inner membrane potential of mitochondria. If mitochondrial membrane potential is decreased due to certain biological events, the mitochondria targeting ability of these sensors will decrease, disfavoring the mitochondrial Zn^{2+} imaging. Different from the sensors based on lipophilic cations, genetically-encoded Zn^{2+} sensors showed major advantages on mitochondria targeting without any dependence on the membrane potential.[99] It is necessary to ensure expression of the sensors does not disrupt the structure and function of the organelles. A number of genetically-encoded Zn^{2+} sensors of mitochondria-targeting ability were reported by Palmer and co-workers, whose mitochondria-targeting sequence at N-terminus is responsible for their mitochondria targeting ability.[91, 163] Ratiometric Zn^{2+} imaging with genetic-encoded FRET sensor was realized with mito-ZapCY-1. Co-localization study with MitoTracker Red showed Pearson's correction coefficients of up to 0.94 in various cell lines (Fig. 30). The RLS procedure displayed a reversible Zn^{2+} imaging ability in HeLa cells. In addition, the intracellular calibration was performed and the free Zn^{2+} level in mitochondria was estimated to be 0.14 pM according to the following formulae: $[Zn^{2+}]=K_d'(R-R_{min})/(R_{max}-R)$.

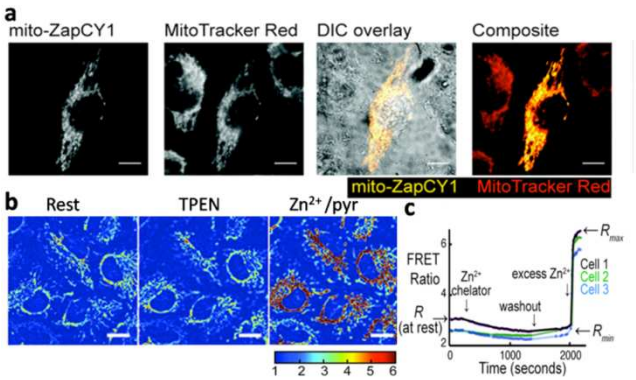

Fig. 30 (a) Co-localization study of mito-ZapCY1 and MitoTracker Red in living HeLa cells. Scale bars, 10 μm. (b) Pseudocolor images of the emission ratio of mito-ZapCY1 in HeLa cells, illustrating changes in the FRET ratio in response to treatment with TPEN or with Zn^{2+}/pyrithione. (c) Temporal profiles of the FRET ratios in living HeLa cells in response to various treatments. Adapted from ref. 163.

Developing genetic/synthetic hybrid sensors is another strategy for tagging a molecular cargo to a specific subcellular localization.[164, 165] Genetically-encoded component was first expressed in a specific organelle, follow by conjugation with an exogenous synthetic sensor. Lippard and co-workers reported a human O^6-alkylguanine transferase (AGT) labelling methodology for directing a Zn^{2+} sensor into mitochondria.[166] ZP1BG was synthesized and used as a substrate for AGT, which was fused in the mitochondria of HeLa cells. Fine co-localization between ZP1BG and MitoTracker Red and mitochondrial Zn^{2+} fluctuation

was revealed (Fig. 31).

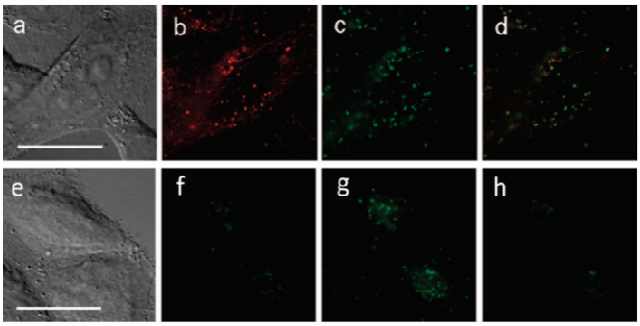

Fig. 31 (a-d): Colocalization study in living HeLa cells expressed with AGT in mitochondria. (a) Bright field image; (b) fluorescence image of MitoTracker Red; (c) fluorescence image of ZP1BG. (d) Overlay of (b) and (c). Bright field image (e) and the related fluorescence images of the living HeLa cells expressing AGT in mitochondria labelling with ZP1BG before (f) and after (g) addition of Zn^{2+}/pyrithione, followed by treatment with TPEN (h). Scale bar, 25 μm. Adapted from ref. 166.

5.2 Lysosomal Zn^{2+} imaging

Lysosomes contain various acidic hydrolases serve as the main sites for macromolecule degradation.[167] Zn^{2+} appears to be a link between oxidative stress and lysosomal membrane permeabilization (LMP).[160] Fluorescent Zn^{2+} sensors for lysosomal Zn^{2+} study is developed to study the lysosomal Zn^{2+}-related oxidative stress and downstream markers for LMP.[168] Considering the acidic pH of lysosomes (4.5−6.0), weakly basic aliphatic amines tend to accumulate in lysosomes through lysosomotropism process.[169,170]

It is worth noting that the interference from proton should be concerned when designing the Zn^{2+} sensors especially the PET based ones. Protonation of the electron donor (usually as Zn^{2+} chelator) could also induce a fluorescence enhancement, which will lead to false signaling. To minimize the interference from proton in lysosomal Zn^{2+} imaging, a Zn^{2+} sensor should have a lower pK_a which keeps its fluorescence unchanged even in a slightly acidic environment.[78] For the regulation Zn^{2+} sensor pK_a, reader are suggested to refer to the reviews about ZP and ZnAF families.

Jiang and co-workers reported an early approach for ratiometric Zn^{2+} imaging in lysosome,[171] using a ratiometric Zn^{2+} sensor DQZn4 which composed of a quinoline scaffold and a targeting anchor dimethylethylamino group. Upon Zn^{2+} binding, this sensor exhibited a significant turn-on response with the concomitant fluorescence ratio alteration due to an emission blue shift of 47 nm. DQZn4 was shown to be able to localize in lysosomes and respond to exogenous and endogenous lysosomal Zn^{2+} fluctuation in living cells.

A BODIPY based ratiometric sensor **LysoZn-1** for lysosomal Zn^{2+} imaging was recently reported by Peng and Fan et al.[172] Its lysosome targeting property was achieved by deriving styryl-BODIPY-DPA scaffold with a 2-morpholinoethylamine targeting moiety. **LysoZn-1** exhibited a blue shift from 680 to 578 nm with a concomitant emission enhancement at 578 nm upon Zn^{2+} binding. **LysoZn-1** was found to localize in lysosome in various cells lines including neural stem cells (NSCs), MCF-7 and HeLa cells with a reversible lysosomal Zn^{2+} imaging ability (Fig. 32). Endogenous lysosomal Zn^{2+} increment triggered by H_2O_2 stimulation in NSCs was also monitored using **LysoZn-1** in a ratiometric manner.

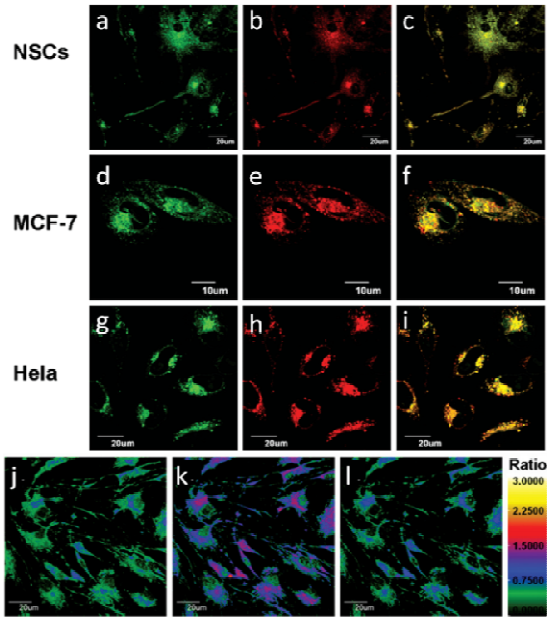

Fig. 32 Fluorescence co-localizations study of LysoZn-1 to lysosomes in NSCs (a–c), MCF-7 (d–f) and HeLa (g–i) cells. (a, d, g) Fluorescence images of LysoSensor Green; (b, e, h) fluorescence images of LysoZn-1; (c, f, i) overlay images of Lysosensor Green image and LysoZn-1 image. Ratio images of the LysoZn-1-stained NSCs before (j) and after (k) Zn^{2+}/pryithione incubation, followed by TPEN treatment (l). Adapted from ref. 172.

5.3 Imaging Zn^{2+} at cell membrane

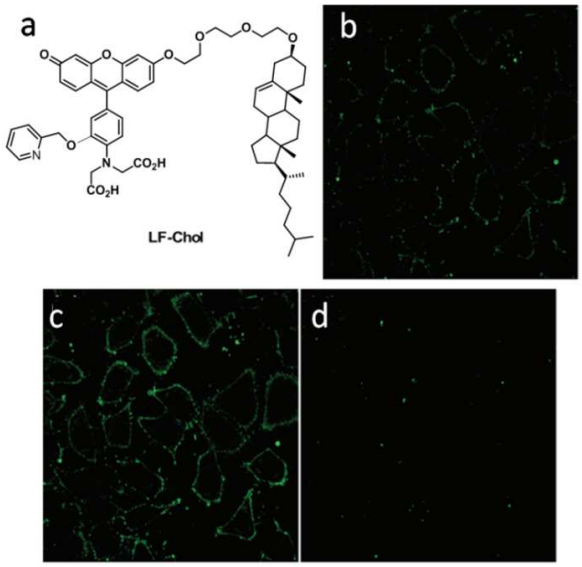

Fig. 33 (a) Chemical structure of LF-Chol. Fluorescence images of HeLa cells stained with LF-Chol before (b) and after (c) the addition of exogenous Zn^{2+}, and followed by EDTA addition (d). Adapted from ref. 173.

Imaging labile Zn^{2+} at cell membrane is crucial for investigating the equilibrium between intracellular and extracellular Zn^{2+}, which requires sensors of cell membrane-targeting ability. Cholesterol tail or long alkyl chains are common targeting groups to anchor cell membrane via strong hydrophobic affinity to

membrane lipids. Membrane Zn^{2+} imaging with LF-Chol was reported by Taki and co-workers.[173] In LF-Chol, a TEG-cholesterol moiety was conjugated with a fluorescein platform. Owing to high hydrophilicity of two carboxyl groups of its Zn^{2+} chelator, Zn^{2+} sensing moiety was expected to be located at the extracellular region in the vicinity of the plasma membrane. As shown in Fig. 33, its membrane targeting ability was confirmed together with the reversible Zn^{2+} imaging ability in a RLS imaging procedure. Another membrane anchored sensor bearing two lipophilic alkyl chains, ZIMR, was also reported to display the turn-on response specifically to Zn^{2+}.[174] With targeting ability to the extracellular region of plasma membrane, ZIMR was utilized to image Zn^{2+}/insulin release of intact rat islets, which revealed the "secretory unit" formed by the small groups of adjacent β cells.

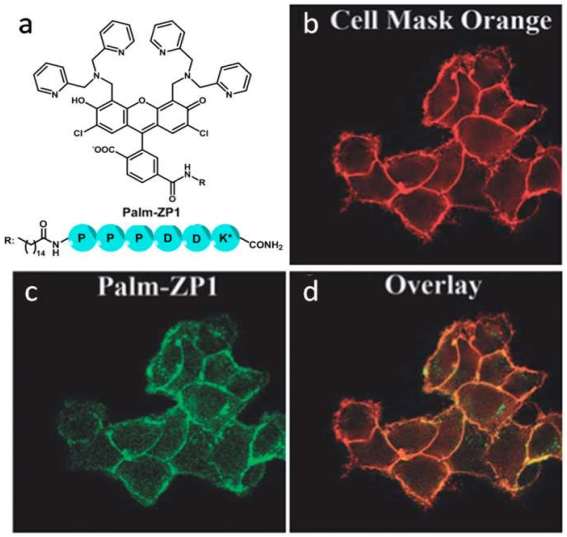

Fig. 34 (a) Chemical structure of Palm-ZP1. (b-d) Co-localization study of Palm-ZP1 in live HeLa cells co-stained with Cell Mask Orange. (b) Fluorescence images of HeLa cells based on the fluorescence of Cell Mask Orange; (c) fluorescence image of cells based on the fluorescence of zinc-bound Palm-ZP1; (d) Overlay image of (b) and (c). Adapted from ref. 175.

By integrating a short peptide PPPDDK with ZP1 or ZQ, new Zn^{2+} sensors, Palm-ZP1 and Palm-ZQ, were obtained extracellular Zn^{2+} imaging at plasma membrane.[175] The palmitoyl moiety mimics the palmitoylation to direct the sensors to the plasma membrane, while the hexapeptide chain separates the palmitoyl terminal from the Zn^{2+} sensing units to retain the fluorescence quantum yield and targeting ability. Palm-ZP1 was found to localize in plasma membrane with a Pearson's correction coefficient of 0.70 (Fig. 34). Palm-ZP1 and Palm-ZQ were used to monitor the changes of extracellular Zn^{2+} level.

Ratiometric Zn^{2+} imaging around cell membrane was realized with a genetically encoded Zn^{2+} sensor, in which CFP and YFP were adopted as energy donor and acceptor fluorophores and bridged with a Zn^{2+} chelating peptide His_4.[91] Localization of the sensor in plasma membrane was confirmed although it only showed low Zn^{2+} affinity with an apparent K_d' of *ca.* 200 μM.

5.4 Imaging Zn^{2+} in Golgi apparatus

Zn^{2+} sensors with selected localization in Golgi or a Golgi-associated vesicle, ZP1, ZP2, ZP3 and QZ2E, have been designed based on fluorescein platform. However, the mechanism for the specific localization of these fluorescein-based sensors in Golgi apparatus is not clear. AGT labelling methods were also successfully used to design sensors for Zn^{2+} imaging in Golgi apparatus.[163]

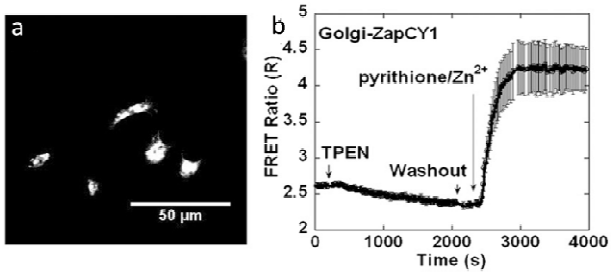

Fig. 35 (a) Fluorescence image of Golgi-ZapCY1 stained HeLa cells. (b) Temporal profile of FRET ratio in HeLa cells visualized by Golgi-ZapCY1. Adapted from ref. 89.

Ratiometric imaging of Zn^{2+} in Golgi was realized by Palmer and co-workers with genetic encoded FPs based sensors (Fig. 35).[89] A FRET-based ratiometric Zn^{2+} sensor ZapCY1O was obtained by optimization of the first and second zinc fingers of *Saccharomyces cerevisiae* Zap1 to bridge two fluorescent proteins, ECFP and EYFP. Zn^{2+} binding induces a conformational change of the two zinc fingers, leading to an increase in FRET from CFP to YFP. By encoding Golgi-ZapCY1 in the inner membrane of Golgi via the targeting sequence, labile Zn^{2+} level in Golgi apparatus of HeLa cells is determined to be 0.6 ± 0.1 pM which was increased when cytosolic Zn^{2+} level was elevated by exogenous Zn^{2+} incubation.

5.5 Imaging Zn^{2+} in endoplasmic reticulum (ER)

Physiological functions of ER include protein folding in cisternae and the transport of the synthesized proteins. Accumulation and aggregation of misfolded proteins in the ER was found related to a number of neurodegenerative disorders.[176, 177] It has been reported that the deletion of zinc transporters and zinc deficiency in the ER could up-regulate unfolded protein responses (UPR).[178]

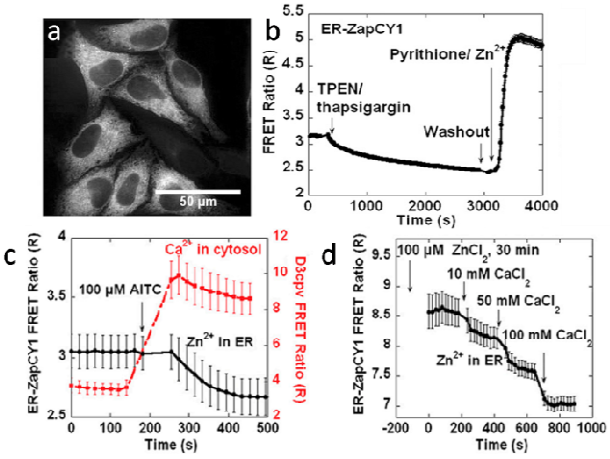

Fig. 36 (a) ER localization of ER-ZapCY1. (b) Temporal profile of FRET ratio in HeLa cells upon treatment with TPEN/thapsigargin and pyrithione/Zn^{2+} in sequence traced by ER-ZapCY1. (c) AITC induced increase of cytosolic Ca^{2+} showed as the FRET ratio of D3cov FRET ratio and the decrease of ER Zn^{2+} showed as the FRET ratio of ER-ZapCY1 in cells. (d) Extracellular Ca^{2+} induced decrease of ER Zn^{2+} monitored by

ER-ZapCY1 showed as the FRET ratio of ER-ZapCY1. Adapted from ref. 89.

ER targeting small molecule Zn^{2+} sensors are rare due to the lack of effective anchoring group. Genetic encoding technology therefore becomes an effective way for the construction of FPs-based FRET sensor for Zn^{2+} in ER. It was reported that Zn^{2+} fluctuation and quantification of labile Zn^{2+} in ER could be monitored using ratiometric Zn^{2+} imaging with FPs-based sensors (Fig. 36).[89] With a similar sensor construction strategy to Golgi-ZapCY1, ER-ZapCY1 were genetically encoded onto lumen of the ER. The ratiometric imaging results disclosed that labile Zn^{2+} level in ER of HeLa cells at the steady state was estimated to be 0.9 ± 0.1 pM which rose to higher level when cytosolic Zn^{2+} level was elevated to nanomolar range. Compared to Ca^{2+} tracking via detection with FPs-based FRET sensor D3cov FRET, Zn^{2+} imaging via ER-ZapCY1 upon AITC treatment revealed that AITC induced increase of cytosolic Ca^{2+} was followed by an ER Zn^{2+} decrease. Free ER Zn^{2+} level was reduced upon cytosolic Ca^{2+} elevated, indicating a connection of ER Ca^{2+} stores and Zn^{2+} dynamics. Ratiometric imaging of Zn^{2+} in ER with this sensor provides direct evidence of the interplay between Zn^{2+} homeostasis and Ca^{2+} signalling.

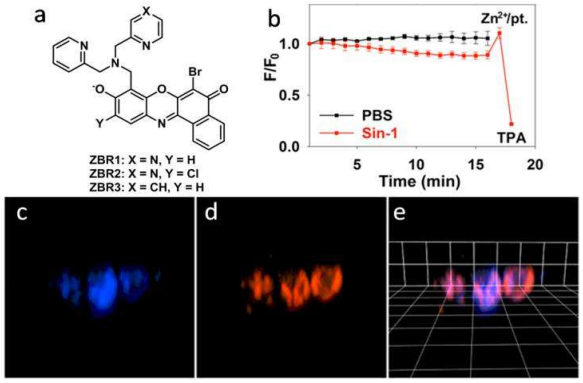

Fig. 37 (a) Chemical structures of ZBR sensors. (b) Fluorescence intensity change of ZBR1 stained NSCs upon different treatment. (c-e) 3D fluorescence image of NSCs co-stained by ER-Tracker and ZBR1. (c) 3D fluorescence image of NSCs based on the fluorescence of ER-Tracker; (d) 3D fluorescence image of NSCs based on the fluorescence of ZBR1; (e) overlay of (c) and (d). Adapted from ref. 179.

Small molecular ER Zn^{2+} sensors derived from benzoresorufin (ZBR) were recently reported by Lippard et al.[179] For example, ZBR1-3 displayed up to 8.4-fold emission enhancement upon Zn^{2+} binding with K_d values in the sub-nanomolar and picomolar ranges. Localization of the sensor in ER was confirmed by reconstructed 3D images. As shown in Fig. 37, ZBR1 can be used to monitor Zn^{2+} release from ER in neural stem cells stimulated by peroxynitrite generator Sin-1. Correlation between ER stress and ER Zn^{2+} homeostasis can be made based on the results. This is also one of the very few examples of 3D reconstructed Zn^{2+} imaging obtained from a series of confocal images using Z-axis scanning.

5.6 Nuclear Zn^{2+} imaging

Zn^{2+} plays essential roles in numerous nuclear proteins such as transcription factors, polymerases, and DNA remodeling factors.[180,181] However, most of the reported intracellular Zn^{2+} imaging showed very week or no fluorescence in nucleus even after treatment with exogenous Zn^{2+}, indicating that most of the reported Zn^{2+} sensors were not able to penetrate into nucleus. Newport Green,[182] and Zinquin[143] are among the very few examples displaying an even intracellular distribution pattern in specific cell lines.

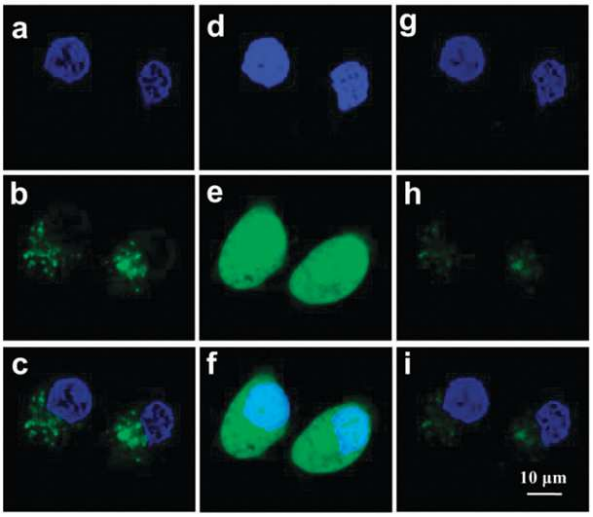

Fig. 38 Confocal fluorescence images of living HeLa cells co-stained with Hoechst 33342 and Naph-BPEA. (a–c): Fluorescence images of the co-stained cells; (d–f): Fluorescence images of the co-stained cells followed by Zn^{2+}/pyrithione incubation; (g–i): Fluorescence images of Zn^{2+}-incubated cells treated further by TPEN. (a), (d) and (g): The fluorescence images of Hoechst (blue channel). (b), (e) and (f): The fluorescence images of Naph-BPEA (green channel). (c), (f) and (i): overlays of the related blue/green channel images. Adapted from ref. 183.

By conjugating a Zn^{2+} chelator N,N'-bis(pyridin-2-ylmethyl)ethane-1,2-diamine (BPEA) with an 1,8-naphthalimide (ANaph) fluorophore, we constructed a Zn^{2+} imaging agent Naph-BPEA with nuclear envelope penetrability.[183] The nuclear envelope penetrability and nuclear Zn^{2+}imaging ability of Naph-BPEA were confirmed by co-staining cells with Naph-BPEA and nucleus dye Hoechst 33342 using LCSM (Fig. 38). In contrast, its analogue NBD-BPEA with a NBD fluorophore to replacing ANaph (see section 6.2) exhibited no distribution in nuclear, indicating that ANaph fluorophore might be the origin for the nuclear envelope penetrability. In fact, strong DNA binding ability of ANaph group was suspected to be the driving force for the nuclear selectivity.[184,185] This sensor did not exclusively localize in cell nucleus, it also fluoresced in cytoplasm. This raised the possibility for simultaneous monitoring of cytosolic and nuclear Zn^{2+} using this sensor.

Ratiometric imaging for nuclear Zn^{2+} with small molecular sensor has not been reported so far. FPs-based ratiometric nuclear Zn^{2+} sensors with FRET response will be discussed in the following section.

5.7 Multicolour subcellular Zn^{2+} imaging

Zn^{2+} sensors with different subcellular targeting abilities and different emission bands have been developed, making it possible for imaging labile Zn^{2+} in different organelles simultaneously via the multi-channel mode. These studies could provide more information on Zn^{2+} homeostasis in different subcellular compartments and help to elucidate inter-organelle events

involved in Zn^{2+} homeostasis. Minimization of spectral overlap between different imaging channels is a key issue to conduct multicolour Zn^{2+} imaging in living cells.

Simultaneous monitoring of cytosolic and mitochondrial Zn^{2+} in HeLa cells was provided by a dual-colour Zn^{2+} imaging using TPM imaging.[186] Cells were co-stained with BZn-Cyto, a cytosol uniformly distributed Zn^{2+} sensor, and FZn-Mito, a mitochondria-targeting Zn^{2+} sensor. Both sensors displayed a fine TPEF upon TP excitation at 750 nm. TPEF from BZn-Cyto channel (400-450 nm) was collected to monitor the cytosolic Zn^{2+} fluctuation, while that from FZn-Mito channel (550-650 nm) was collected to monitor the mitochondrial Zn^{2+} fluctuation. When HeLa cells were treated by DTDP, an increase of Zn^{2+} level in both cytosol and mitochondria was induced, whereas a decrease of Zn^{2+} level in both cytosol and mitochondria was observed when treated by CCCP (Fig. 39). It was also noted that cytosolic Zn^{2+} level fluctuated almost simultaneously with mitochondrial Zn^{2+}, and the mitochondria regulating agents such as DTDP and CCCP were able to regulate cytosolic Zn^{2+} level.

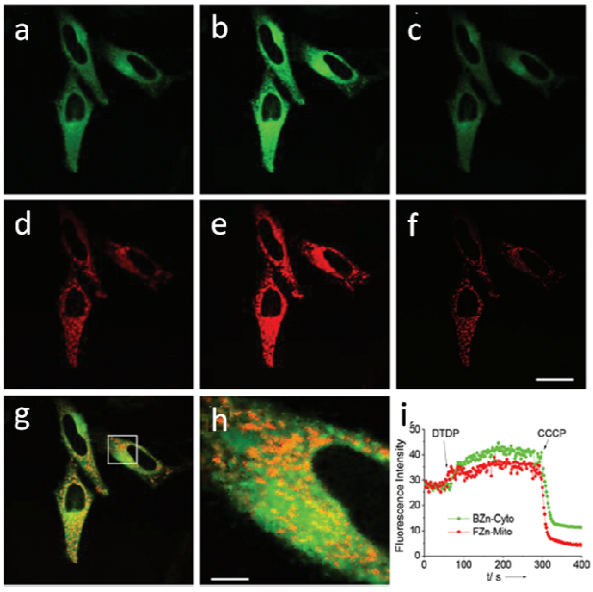

Fig. 39 TPM fluorescence images of HeLa cells co-stained with BZn-Cyto and FZn-Mito obtained from Ch1 (BZn-Cyto channel, 400-450 nm, a–c) and Ch2 (FZn-Mito channel, 550-650 nm, d–f). TPM images were collected before (a, d) and after (b, e) addition of DTDP, followed by addition of CCCP (c, f). (g) Merged image of (a) and (d). (h) The zoomed image of region of interest shown as the white box in (g). (i) Relative TPEF intensity of HeLa cells co-stained with BZn-Cyto and FZn-Mito at different time course. The excitation wavelength was 750 nm. Scale bars: (f) 30 and (h) 5 μm. Adapted from ref. 186.

Simultaneous ratiometric Zn^{2+} imaging in different organelles has also been reported by Palmer et al. using a genetic encoded method (Fig. 40).[187] Labile Zn^{2+} in multiple subcellular locations could be monitored using a series of FPs-based FRET Zn^{2+} sensors. For example, Zn^{2+} level was tracked respectively in a pair of organelles such as nucleus/cytosol, nucleus/ER, nucleus/Golgi, nucleus/mitochondria. Dual colour ratiometric imaging requires two ratiometric Zn^{2+} sensors constructed by two FRET FP pairs respectively, and four emission channels were detected simultaneously to obtain two emission ratios for nucleus and the other organelle. Therefore, two donating/accepting FP pairs of FRET effect should be carefully tuned to minimize emission overlap among the four FPs. Simultaneous ratiometric imaging of Zn^{2+} in nuclear and cytosol revealed that cytosol and nucleus accumulated Zn^{2+} with comparable rates upon incubation with $ZnCl_2$ solution. In addition, ratiometric imaging for Zn^{2+} uptake in nucleus/ER, nuclear/mitochondria and nucleus/Golgi pairs upon Zn^{2+} incubation demonstrated that nuclear took up Zn^{2+} fast, while ER, Golgi, and mitochondria all sequestered Zn^{2+} in a slower rate with a delay of 600–700 sec.

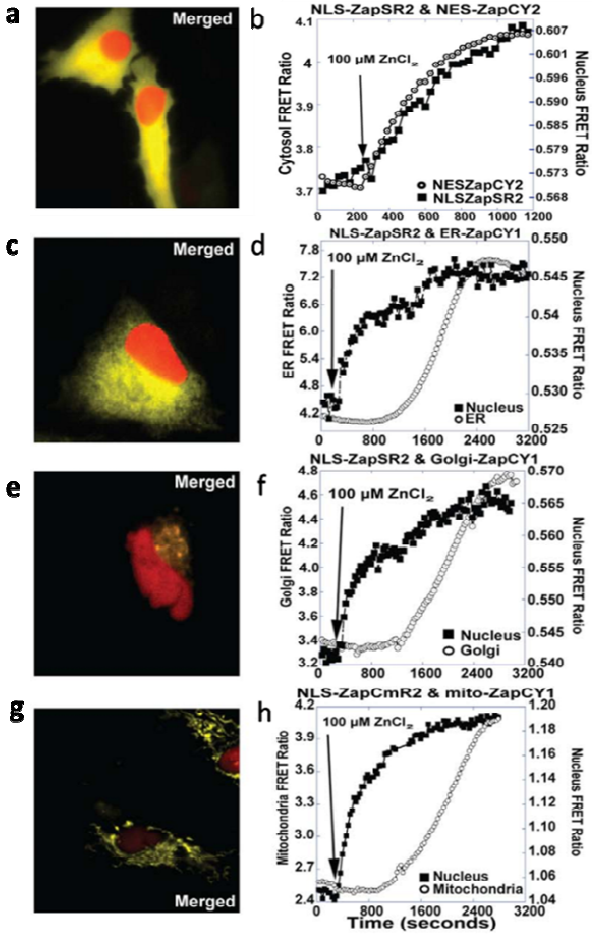

Fig. 40 (a) Simultaneous imaging for nuclear and cytosolic Zn^{2+} in the same cells expressed with both NLS-ZapSR2 and NES-ZapCY2. (b) Temporal profile of FRET ratios of NLS-ZapSR2 and NES-ZapCY2 detected in cells upon $ZnCl_2$ (100 μM) incubation. (c) Simultaneous imaging for nuclear and ER Zn^{2+} in the same cell expressed with both NLS-ZapSR2 and ER-ZapCY1. (d) Temporal profile of FRET ratios of NLS-ZapSR2 and ER-ZapCY1 detected in cells upon $ZnCl_2$ (100 μM) incubation. (e) Simultaneous imaging for nuclear and Golgi Zn^{2+} in cells expressed with both NLS-ZapSR2 and Golgi-ZapCY1. (f) Temporal profile of FRET ratios of NLS-ZapSR2 and Golgi-ZapCY1 detected in cells upon $ZnCl_2$ (100 μM) incubation. (g) Simultaneous imaging for nucleus and mitochondrial Zn^{2+} in the same cells expressed with both NLS-ZapCmR2 and mitochondria-ZapCY1. (h) Temporal FRET ratios of NLS-ZapCmR2 and mitochondria-ZapCY1 detected in cells upon incubation with $ZnCl_2$ (100 μM). Adapted from ref. 187.

6. Zn^{2+} imaging in tissues and live animal modes

6.1 Zn^{2+} imaging in tissues

Due to high level of labile Zn^{2+}, rat brain tissue slices were the

most commonly studied tissue for Zn^{2+} imaging. The first histological Zn^{2+} imaging was demonstrated in mouse hippocampus slices using TSQ.[61] Zn^{2+}-riched regions such as hilus of the dentate gyrus and mossy fibers of hippocampus exhibited a distinct fluorescence (Fig. 41). These fluorescence images were collected upon UV excitation using widefield fluorescence microscopy, therefore, the effective spatial resolution was limited to about 15 μm and imaging depth within 60 μm. A TSQ derivative TFLZn was used to image Zn^{2+} in the brain slices of 10 μm, which confirmed the contribution of synaptic Zn^{2+} to the accumulation of amyloid plaques in Alzheimer's disease.[188]

A visible light excitable sensor, Newport Green DCF, was applied to visualize the release of Zn^{2+} from presynaptic terminals.[27, 189] Under electrical stimulation, Zn^{2+} was immediately released from synaptic terminals into the synaptic cleft, then entered postsynaptic neurons and increased the intracellular Zn^{2+} concentration. The results indicated that mossy fiber Zn^{2+} release was correlated to the induction of long-term potentiation (LTP) at mossy fiber to CA3 synapses.

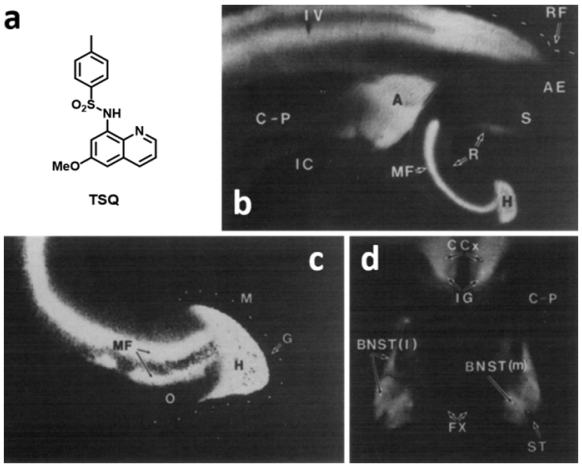

Fig. 41 (a) Chemical structure of TSQ. Widefield fluorescence images of (b) horizontal section of the mouse brain after staining in TSQ and clearing in glycerine. (c) Horizontal section of mouse hippocampus stained with aqueous TSQ. (d) Horizontal section of the mouse brain. Abbreviations: A, amygdala; AE, entorhinal cortex; C-P, caudate-putamen; G, granule cell stratum of dentate gyrus; H, hilus of the dentate gyms; IC, internal capsule; M, molecular zone of dentate gyms; MF, mossy fibers of hippocampus; O, stratum oriens; R, stratum radiatum of hippocampus; S, subiculum; IV, lamina IV of neocortex; BNST, bed nucleus of the stria tenninalis, pars medialis (m) and lateralis (L): C-P caudale/putamen; IG, induseum griseum; CCX. cingulale cortex; FX. fornix, descending columns; ST, stria terminalis. Adapted from ref. 61.

Turn-on fluorescence Zn^{2+} imaging in tissues suffers similar problems as in intracellular Zn^{2+} imaging. Moreover, slice variation in tissue homogeneity and thickness leads to even more artifacts in turn-on imaging. Ratiometric imaging for Zn^{2+} in tissue can help minimize these interferences and improve the image quality, while the long excitation wavelength should be also helpful to improve the imaging effectiveness. Ratiometric imaging for endogenous Zn^{2+} in rat hippocampal slices was obtained using a visible light excitable iminocoumarin sensor ZnIC.[190] The emission maximum of ZnIC shifted from 543 to 558 nm upon Zn^{2+} binding with a K_d of 1.3 pM. The dentate gyrus, CA3, and CA1 regions, where contain glutamatergic neurons rich in vesicular zinc, showed a distinct higher ratios in ratiometric imaging. High ratio value in these regions was reduced to background signal level when treated with TPEN (Fig. 42d). The intensity-based fluorescence images showed a bright region in their left lower region (Fig. 42b-c), which displayed as the background ratio signal in ratiometric images (Fig. 42d). This result suggested that background fluorescence in tissue can be effectively removed via ratiometric imaging. Moreover, the fluorescence intensity of the hippocampal silces stained with intensity based Zn^{2+} sensor ZnAF-2 gradually decreased during the imaging course due to photobleaching (Fig. 42e), while the ratiometric image based on ZnIC-staining was stable. All these results demonstrated distinct advantages of ratiomertic imaging over turn-on imaging in tissues.

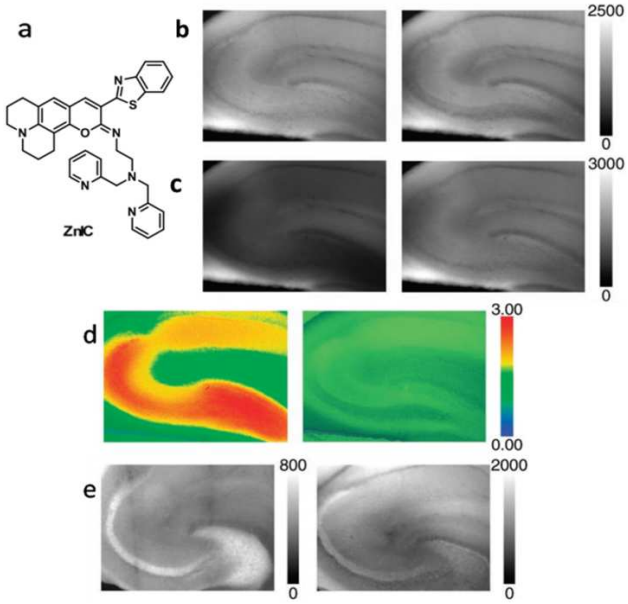

Fig. 42 (a) Chemical structure of ZnIC. (b) Fluorescence images of a ZnIC-stained rat hippocampal slice based on the emission collected at 565-605 nm before (left) and after (right) incubation with TPEN. (c) Fluorescence images of a ZnIC-stained rat hippocampal based on the emission collected at 510-550 nm before (left) and after (right) incubation with TPEN. (d) Ratio images generated form (b) and (c). (e) Fluorescence images of rat hippocampal slices stained with turn-on Zn^{2+} sensor ZnAF-2 at different time course. Adapted from ref. 190.

The 3D information of labile Zn^{2+} in tissue could be acquired by LCSM and TPM due to their optical sectioning ability. Since TPM imaging provides higher spatial resolution with improved S/N ratio, longer imaging time, deeper tissue penetration as well as 3D visualization, Zn^{2+} sensors with large TP action cross-section (Φδ) are highly preferable to visualize labile Zn^{2+} in tissues via TPM imaging. The most commonly used TP fluorophores for Zn^{2+} imaging are fluorescein, benzoxazole, stilbene, quinoline derivatives and naphthalene derivatives, which showed Φδ values varied from 50 to 580 GM in the presence of Zn^{2+}.

TPM Zn^{2+} imaging in acute mouse hippocampal slices achieved using a fluorescein based sensor, ZP3.[191] Bright fluorescence was observed in the hilus of dentate gyrus and the stratum lucidum of CA3 region upon excitation at 800 nm with a pulsed laser. Moreover, stratum lucidum layer and individual

giant mossy fiber boutons could be resolved in the images with higher magnification (Fig. 43).

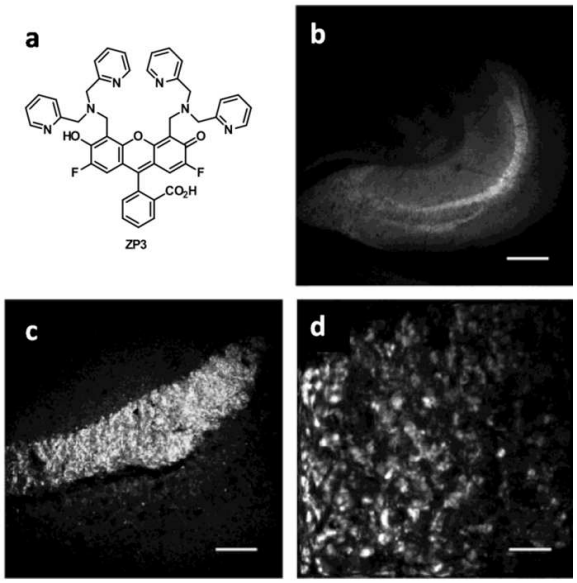

Fig. 43 (a) Chemical structure of ZP3. (b-d) TPM image of an acute mouse hippocampal slice stained with ZP3. (b) Magnification at 10× showed an entire slice section of a mouse hippocampus with all of the different Zn^{2+}-containing cytoarchitectonic regions; scale bar: 200 μm. (c) Magnification at 40× highlighted the stratum lucidum layer; scale bar: 50 μm. (d) Magnification at 200× resolved the individual giant mossy fiber boutons; scale bar: 10 μm. Adapted from ref. 191.

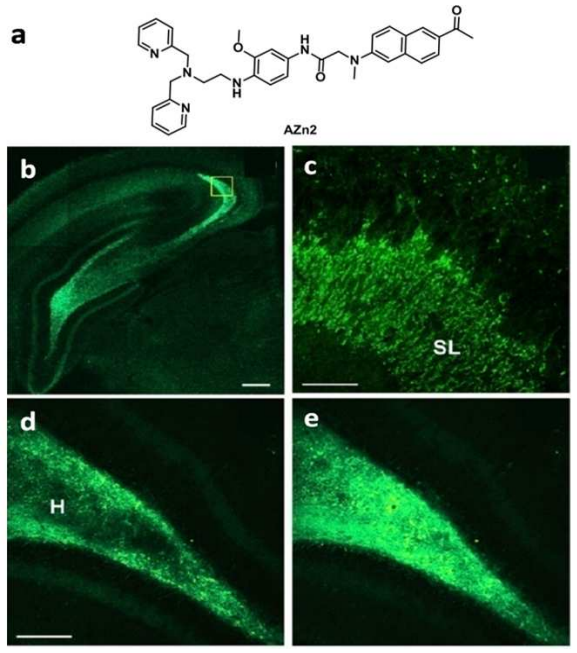

Fig. 44 (a) Chemical structure of AZn2. (b-e): TPM images of the rat hippocampal slice stained with AZn2. (b) TPM image at a depth of ~120 μm with magnification 10×. (c) Magnification at 100× in SL of CA3 regions (yellow box) at a depth of ~100 μm. TPM images in H of DG regions at a depth of ~100 μm before (d) and after (e) KCl addition to the imaging solution. Scale bars: 300 μm in (b) and (d); 150 μm in (c). Adapted from ref. 192.

With 2-acetyl-6-(dimethylamino)-naphthalene (Acedan) as parent fluorophore of TPEF , a series of turn-on TP Zn^{2+} sensors with various K_d values ranging from sub-nanomolar to sub-millimolar were developed.[192, 193] The TPEF intensity of the sensors was increased by up to 54 folds upon addition of Zn^{2+}. Most of these sensors such as AZn1 and AZnE2 showed $\Phi\delta_{TPA}$ values of ~90 GM upon excitation with pulsed laser at 780 nm suitable for TPM imaging. TPM imaging of a fresh rat hippocampal slice labelled with AZn2 demonstrated bright regions in the stratum lucidum (SL) of CA3 and the hilus (H) of dentate gyrus (DG) (Fig. 44). Moreover, the TPEF was increased upon treatment with KCl, a membrane depolarizer that causes the release of Zn^{2+} (Fig. 44d-e). A decrease of TPEF was observed in the followed treatment with TPEN. The RSS imaging procedure for labile Zn^{2+} imaging in tissues suggested a reversible TPM imaging ability of this sensor for Zn^{2+} in tissues. Moreover, the result indicated that the intracellular Zn^{2+} in the SL of CA3 regions was mainly accumulated in mossy fiber axon terminals of pyramidal neurons. With this TPEF sensor, endogenous labile Zn^{2+} in tissue can be visualized at a depth of 80−150 μm using TPM imaging.

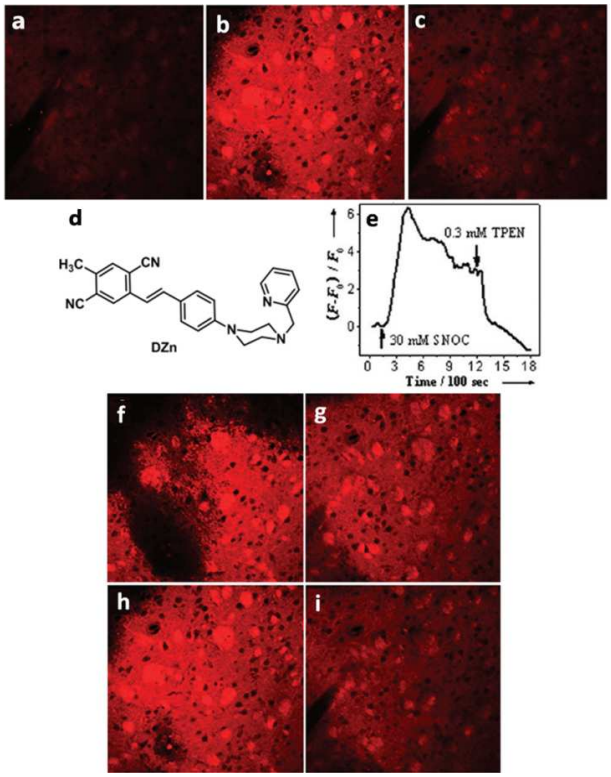

Fig. 45 (a-c): TPM images of a mouse brain tissue slice stained with10 μM DZn at a depth of ca. 120 μm with magnification 100×. The image before and after SNOC (30 mM) treatment was given as (a) and (b) respectively; (c) the image of slice in (b) was treated further with TPEN (0.3 mM). (d) Chemical structure of DZn. (e) The related temporal profile of TPEF detected in (a-c). (f-i): TPM images of the mouse brain tissue slice stained with 10 μM DZn (magnification 100×) at different penetration depths of (f) 80, (g) 100, (h) 120, and (i) 150 μm. The TPEF images were collected via band path of 550-650 nm upon excitation at 810 nm with a femtosecond pulsed laser. Adapted from ref. 194.

A TP sensor for Zn^{2+}, DZn, using dicyanostilbene as the parent fluorophore of TPEF nature was reported by Huang et al.[194] DZn was showed to give a 72.5-fold fluorescence enhancement in response to Zn^{2+} and a considerably large two-photon action cross-section (580 GM) for Zn^{2+} complex. TPM images obtained from a DZn-stained mouse brain tissue slice demonstrated that

the TPEF intensity was enhanced after the addition of SNOC and decreased upon the followed TPEN treatment. This RSS imaging procedure confirmed the reversible imaging ability for labile Zn^{2+}. With the pulsed excitation at 810 nm, the TP fluorescence of the DZn stained mouse brain tissue slice can be retained for 1500 s or so. Moreover, the TPM images at different depth from 80 to 150 μm revealed the labile Zn^{2+} distribution pattern in mouse brain tissue slices along *z* direction (Fig. 45).

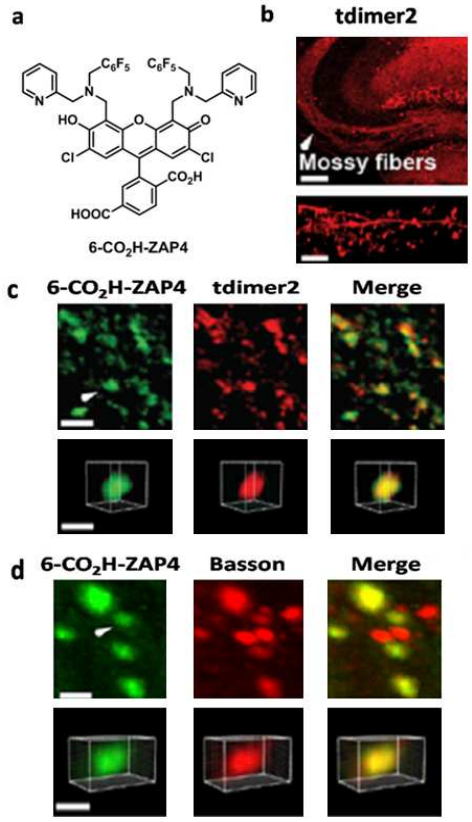

Fig. 46 (a) Chemical structure of 6-CO_2H-ZAP4. (b) Upper: TPM fluorescence image of the mossy fiber region sparsely expressing red fluorescence (tdimer2) in adult hippocampal slices (Thy1-Brainbow 1.0 line H transgenic mouse); Lower: TPM fluorescence image of red fluorescent mossy fibers including boutons in the hippocampal slice. Scale bars: Upper, 100 μm; Lower, 10 μm. (c) Upper: colocalization of 6-CO_2H-ZAP4 (green) and tdimer2 (red) in mossy fiber boutons of a hippocampal slice; Lower: higher magnification 3D view of the mossy fiber boutons indicated by a white arrow. Scale bars: Upper, 5μm; Lower, 2 μm.). (d) Upper: colocalization of 6-CO_2H-ZAP4 (green) and a presynaptic active zone marker, bassoon (red), in a hippocampal slice; Lower: 3D view of the boutons indicated by a white arrow at higher magnification. Presynaptic structures were immunolabeled by bassoon antibody after staining with 6-CO2H-ZAP4. Scale bars: Upper, 5 μm; Lower, 2 μm. Adapted from ref. 195.

A TPM imaging of Zn^{2+} dynamics at individual presynaptic level using sensor 6-CO_2H-ZAP4 was reported recently by Lippard et al. [195] Weak depolarization stimulus induces the fusion of synaptic vesicles that allows this membrane impermeable sensor to enter fused vesicles, and the related TPEF Zn^{2+} imaging of the hippocampal slices showed the high accumulation of sensor in the stratum lucidum layer between the CA3 and DG regions. With the advantage of TPM, the enlarged 3D images with spatial resolution below 2 μm were constructed, which confirmed localization of 6-CO_2H-ZAP4 in presynaptic regions of mossy fiber boutons (Fig. 46). This study demonstrated a TPM imaging of presynaptic Zn^{2+} dynamics in synapse level, which is helpful in improving the understanding of physiological roles of labile Zn^{2+} in regular and aberrant neurologic functions.

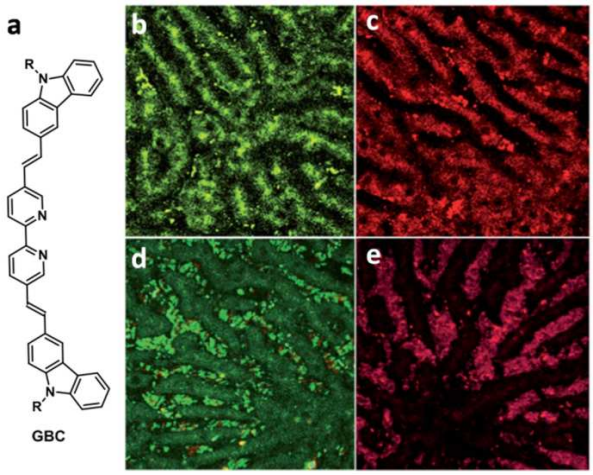

Fig. 47 (a) Chemical structure of GBC. Fluorescence dual channel image of hepatocytes in live rat after intravenous injection with GBC (b, λ_{em}, 530 nm) and GBC-Zn^{2+} (c, λ_{em}, 650nm). TP multispectral images of tissues after intravenous injection with GBC (d, λ_{em}, 500-600 nm) and GBC-Zn^{2+} (e, λ_{em}, 600-700 nm) upon excitation at 820 nm with a pulsed laser. Adapted from ref. 196.

A TPM ratiometric Zn^{2+} imaging in rat liver tissues using a bipyridine centered donor–acceptor–donor (D–π–A–π–D) type sensor, GBC, was reported recently (Fig. 47).[196] In this sensor, the central bipyridine (acceptor) was connected with two carbazole (donor) moieties through vinylic linkages at 5,5-positions of bipyridine. It displayed a Zn^{2+}-induced TPEF shift from 520 to 630 nm, and an enhanced Φδ value from 95 GM to 860 GM. TP tissue imaging in live hepatocytes of rat by a pulsed excitation at 820 nm further confirmed the effectiveness of GBC as a TP Zn^{2+} imaging agent.

6.2 *In vivo* Zn^{2+} imaging in small animal modes

Due to the optical transparent nature and high homology with mammals, zebrafish larvae stand out as the most valuable animal model for *in vivo* fluorescent imaging.[197] Unlike opaque mouse tissue, zebrafish larvae possess minimal light scattering which allows *in vivo* imaging even by visible light excitation.

We have developed the first *in vivo* fluorescence Zn^{2+} imaging in zebrafish larvae with a visible light excitable Zn^{2+} sensor NBD-TPEA. [198] This sensor showed significant fluorescence enhancement in the presence of Zn^{2+}. Fluorescence microscopic Zn^{2+} imaging in zebrafish embryo stained with NBD-TPEA revealed two zygomorphic luminescent areas around its ventricle, which might be related to Zn^{2+} storage for zebrafish development (Fig. 48II a-j). These areas finally disappeared after several days. Moreover, a high concentration of Zn^{2+} in the developing neuromast of zebrafish larvae was observed at higher magnification by confocal fluorescence imaging (Figure 48III a-d). Successful *in vivo* confocal imaging implied a potential of 3D reconstruction based on Zn^{2+} images obtained at different Z-axis. The bright zygomorphic luminescent areas were also observed by Xu and Yoon later on using another visible light excitable turn on Zn^{2+} sensor.[199] A similar in vivo Zn^{2+} imaging of zebrafish

larvae was reported also by Nam et al. using a turn-on Zn^{2+} sensor HNBO-DPA.[200] Watkinson et al. have investigated *in vivo* Zn^{2+} distribution in the eyes, iridophores, gall bladder, pancreas, solitary islet, bile ducts, liver and intestine of zebrafish larvae using a naphthalimide-derived visible light excitable turn-on Zn^{2+} sensor.[201]

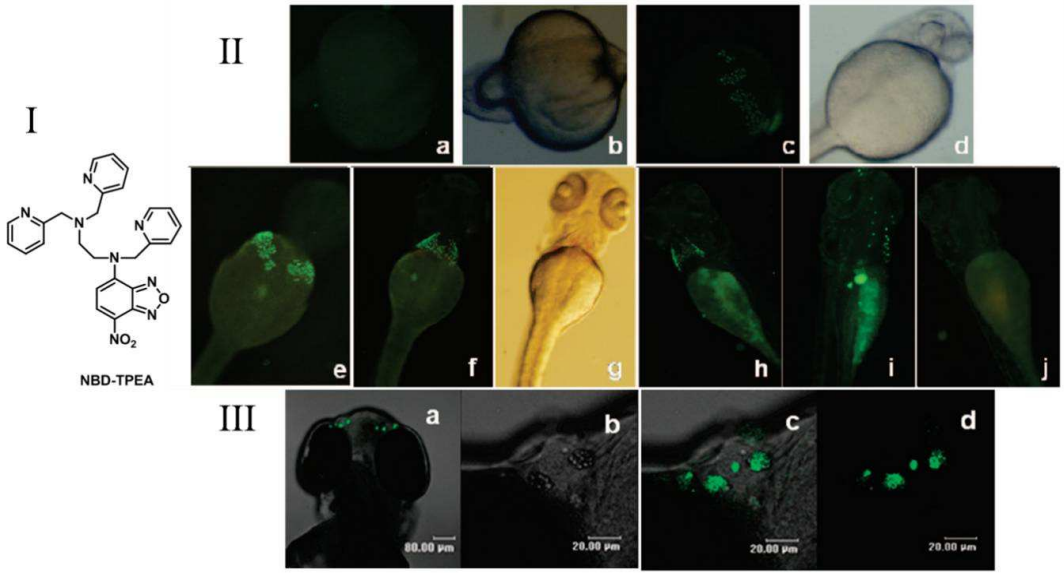

Fig. 48 (I): Chemical structure of NBD-TPEA. (II): Fluorescence microscopic images of zebrafish larva stained with NBD-TPEA. (a) Fluorescence image after 18 hpf; (b) bright-field transmission image of (a); (c) fluorescence image after 25 hpf; (d) bright-field transmission image of (c); (e) fluorescence image after 36 hpf; (f) fluorescence image after 54 hpf; (g) bright-field transmission image of (f); (h) fluorescence image of 5-day-old zebrafish larva; (i) fluorescence image of 7-day-old zebrafish larva; (j) fluorescence image of 5-day-old zebrafish larva after treatment with TPEN. (III): Confocal fluorescence images of the head of a 4-day-old zebrafish larva incubated with Zn^{2+} solution. (a) Co-localization of bright-field and fluorescence images for the head (dorsal view); (b) bright-field image of the left part of the head at higher magnification; (c) co-localization of bright-field and fluorescence images for the left part of the head; (d) fluorescence image of the left part of the head at higher magnification. Adapted from ref. 198.

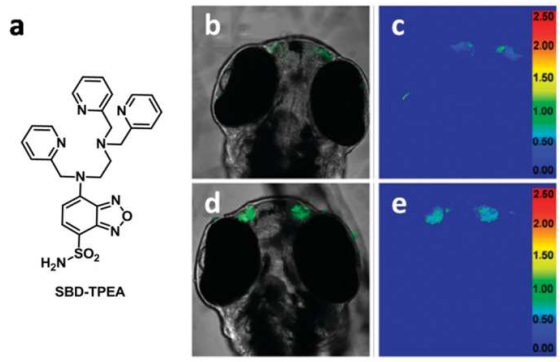

Fig. 49 (a) Chemical structure of SBD-TPEA. (b-e) Confocal fluorescence ratiometric Zn^{2+} imaging in the head of a 3-day-old zebrafish larva stained with SBD-TPEA. (b) Overlay of bright field and fluorescence image of the SBD-TPEA-stained zebrafish larva from the green channel (500-560 nm). (c) Ratiometric image based on the fluorescence images of the zebrafish larva in (b) obtained from the green channel (500-560 nm) and red channel (570-650 nm) . (d) Overlay of bright field and fluorescence image of the SBD-TPEA-stained zebrafish larva from the green channel (500-560 nm) after feeding the larva with Zn^{2+} solution (100 μM) for 1 h. (e) Ratiometric image of the larva in (d) based on the fluorescence images obtained respectively from the green and red channels. Adapted from ref. 202.

Besides the in vivo turn-on Zn^{2+} imaging, we have conducted *in vivo* ratiometric Zn^{2+} imaging of zebrafish larvae. Ratiometric imaging of labile Zn^{2+} in neuromasts of zebrafish larva using a ratiometric sensor SBD-TPEA was realized by confocal microscopy.[202] SBD-TPEA displayed a specific Zn^{2+}-induced emission shift from 585 to 545 nm with a K_d of 2.1 nM. The dual emission mode of ratiometric imaging for SBD-TPEA-stained zebrafish larvae showed a significant enhancement ratio in the ratio image after feeding the larvae with 100 μM Zn^{2+} for 1 h (Fig. 49). A tentative quantification imaging indicated that Zn^{2+} incubation enhanced labile Zn^{2+} level from 1.3 to 10.9 nM in zebrafish neuromasts.

In vivo Zn^{2+} imaging in zebrafish has also been reported by Shin and Yoon using a cyanine based ratiometric Zn^{2+} sensor CTMPA with emission in the red to NIR range.[203,204] Upon Zn^{2+} addition, CTMPA exhibited a large hypsochromic shift from 730 to 590 nm. Bright red fluorescent spots were observed in the bottom of the venter after 24 hpf of the zebrafish embryo, migrated to the top of the venter after 48 hpf and then disappear after 72 hpf (Fig. 50), which is similar to our earlier observation.[1988] Moreover, the bright dots distributed in the head indicated that this sensor was capable of selectively detecting intact endogenous labile Zn^{2+} in zebrafish neuromasts (Fig. 50e). Similar results were also obtained by Pang and co-workers using another NIR Zn^{2+} sensor.[99] Compared to the imaging results reported with visible light excitable Zn^{2+} sensors, the in vivo Zn^{2+} imaging in zebrafish larvae with NIR Zn^{2+} sensors displayed higher S/N ratio due to the low autofluorescence interference.

Live mouse is a more attractive animal model for biological imaging. However, due to the lack of Zn^{2+} sensors suitable for whole body optical fluorescence imaging, fluorescence Zn^{2+} imaging in live mice is challenging. NIR excitation or emission is required to enhance tissue penetration. The spatial resolution of normal optical imaging is limited to 2-3 mm, and the penetration depth is within 1 cm.[205] A pioneer work by Moore and Lippard

reported an in vivo Zn^{2+} imaging in live mice for prostate cancer diagnosis,[206] using a turn-on Zn^{2+} sensor ZPP1. Epifluorescence whole-body optical imaging of prostate Zn^{2+} was obtained. After 30 min from intravenous injection of ZPP1, a careful incision at prostate was made and the anesthetized mouse was then subjected to intravital microscopy. The strong fluorescence was associated with the zinc-rich prostatic glandular epithelium. A progressive loss of fluorescence in transgenic mice was observed during the progression of the prostate adenocarcinoma, indicating the drop of mobile Zn^{2+} concentration in the prostate regions (Fig. 51). These findings supported a prostate-cancer diagnostics using Zn^{2+} as an imaging biomarker. It should be mentioned that the imaging was carried out by excitation at visible light window (~ 500 nm), which may cause atuofluorescence interference and suffers from poor imaging depth. TP and NIR sensors will be able to overcome the obstacles and promise future potential for in vivo optical Zn^{2+} imaging in live mice.

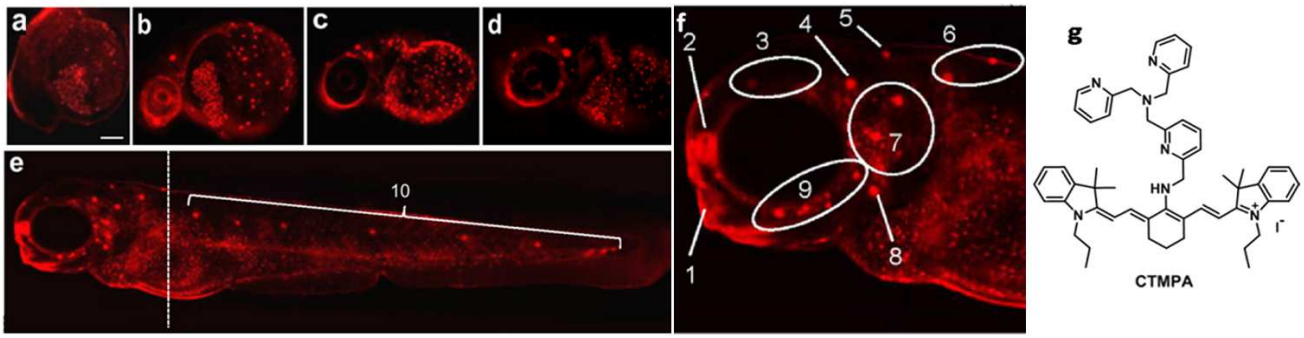

Fig. 50 Confocal fluorescence images of (a) 24 h, (b) 36 h, (c) 48 h, (d) 72 h and (e) 96 h-old zebrafish incubated with CTMPA for 1 h. Scale bar: 20 μM. (f) Enlarged fluorescence image of zebrafish head in (e). 1-10: Different neuromasts. (g) Chemical structure of CTMPA. Adapted from ref. 204.

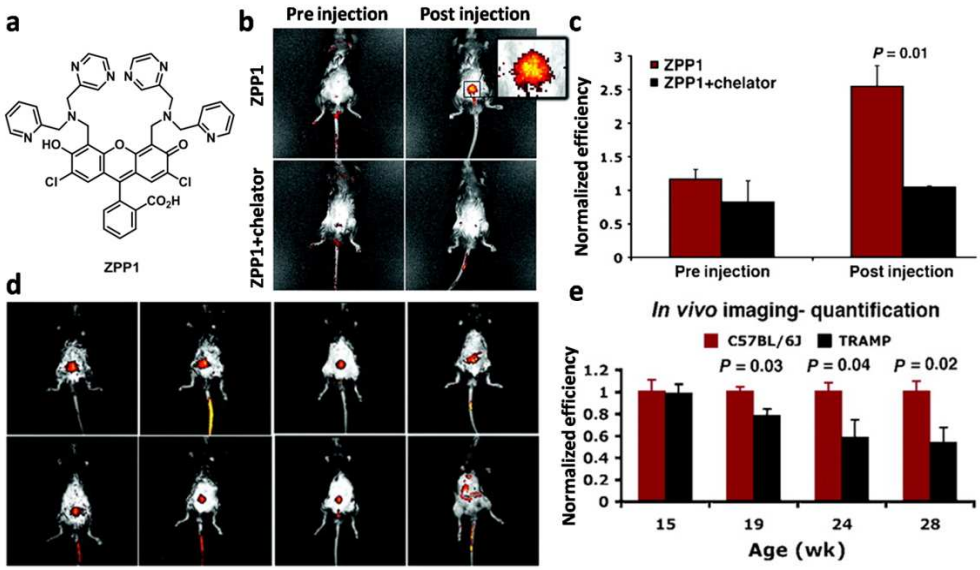

Fig. 51 (a) Chemical structure of ZPP1. (b) Whole-body epifluorescence optical imaging of C57BL/6J mice before (left) and 30 min after (right) tail-vein injection of ZPP1 alone (top) or ZPP1 with chelator TPA (bottom). (c) Quantitative evaluation of (b). (d) Whole-body epifluorescence optical imaging of 15-, 19-, 24-, and 28-week-old C57BL/6J (top, control) and TRAMP (bottom, transgenic) mice 30 min after tail-vein injection of ZPP1. (e) Quantitative evaluation of the fluorescence shown in (d). Adapted from ref. 206.

7. Summary and future remarks

Significant developments have been made in the photoluminescence Zn^{2+} imaging since the first imaging on rat hippocampus slice over two decades ago. A number of different imaging techniques and methods have been adopted, ranging from widefield fluorescence microscopy to confocal microscopy, from single photon fluorescence microscopy to multi-photon fluorescence microscopy, from photoluminescence intensity based imaging to lifetime based imaging. With the advances of these techniques, temporal and spatial information of labile Zn^{2+} could be obtained in cells lines, tissues and organs.

With the great success mentioned above, photoluminescence Zn^{2+} imaging yet faces major challenges. Zn^{2+} imaging in live animal models is unsatisfactory since the number of NIR Zn^{2+} sensors is quite limited. Majority of the existing NIR Zn^{2+} sensors exhibit excitation wavelengths shorter than 650 nm with poor photo-stability. Therefore, developing Zn^{2+} sensors which can operate in the NIR window are of high priority. In this regard, Zn^{2+} sensors based on photo-stable NIR fluorophores or

upconversion nanoparticles (UCNPs)[207,208,209] are preferable for whole body living animal Zn^{2+} imaging. PL imaging shows limited imaging depth (< 1 cm), which requires improvement on NIR sensors as well as new theoretical models for light propagation in tissue. On the other hand, other imaging modalities such as MRI, positron emission tomography (PET) and single-photon emission computed tomography (SPECT) show no limit of imaging depth. Therefore, multimodal imaging techniques combining PL technique with these modalities may be promising alternatives for whole body *in vivo* Zn^{2+} imaging.

For subcellular Zn^{2+} imaging, Zn^{2+} sensors with specific organelle targeting ability are of fundamental importance. The genetic encoded FPs based Zn^{2+} sensors showed great successes in subcellular Zn^{2+} imaging. However, small molecule based Zn^{2+} sensors face difficulty in Zn^{2+} imaging in specific organelles such as ER, Golgi and nucleus. Development of reliable targeting groups for the delivery of Zn^{2+} sensors into these subcellular compartments is appealing. Spatial resolution is another obstacle that limits subcellular Zn^{2+} imaging especially in the single organelles. Super resolution techniques such as stimulated emission depletion (STED), photoactivated localization microscopy (PALM), stochastic optical reconstruction microscopy (STORM) have successfully brought optical microscopy into the nano-dimension.[210, 211] Design of Zn^{2+} sensors suitable for super resolution fluorescence microscopy (SRFM) has a very bright future for exploring Zn^{2+} physiology in single organelle or even at single molecule level.

Acknowledgements

We thank the National Basic Research Program of China (No. 2011CB935800, 2015CB856300) and National Natural Science Foundation of China (No. 21271100 and 10979019, 91213305, 91413116, 21131003, and 21361140352) for financial support. Y. Chen was supported by the Program A for outstanding PhD candidate of Nanjing University (No. 201301A05).

Biography and photograph

Yuncong Chen was born in Chongqing, China. After receiving his BS degree from Nanjing University in 2008, he continued his PhD study in NJU under supervision of Prof. Zijian Guo and Prof. Weijiang He, and got his PhD degree in 2014. He is currently a postdoctoral fellow working with Prof. Benzhong Tang in HKUST. His research interest is focused on the development of photoluminescent probes for the detection and imaging of biological and environmental related species.

Yang Bai was born in Yangzhou, China in 1989. He received his Bachelor's degree from Nanjing Normal University in 2011. Then he enters Nanjing University and started working under supervision of Prof. Weijiang He as a PhD candidate. His research interests include fluorescent probes and their application in bioimaging.

Zhong Han was born in Jinan, China, in 1988. He received his Master's degree in Inorganic Chemistry from Liaocheng University in 2013. He is now doing PhD studies in Nanjing University under the supervision of Prof. Weijiang He. His research interests focus on phosphorescent transition metal complexes, including synthesis and photochemical studies, as well as their applications in bioimaging.

Weijiang He was born in Jiangsu, China in 1969. He received his PhD degree in chemistry from Nanjing University in 2001. After a one year stay as a postdoc in the Max-Planck Institute of Colloids and Interfaces at Potsdam, he joined Nanjing University in 2003 as an associate professor and was promoted to full professor in 2009. His research interests include the fluorescent sensing and imaging of bioinorganic species, photoactive agents,

and luminescent materials.

Zijian Guo was born in Hebei, China in 1961. After receiving his PhD degree from the University of Padua in 1994, he worked as a postdoc at the University of London, the University of British Columbia and the University of Edinburgh successively. He joined Nanjing University in 1999, worked as the director of the State Key Laboratory of Coordination Chemistry from 2000 to 2009. He is currently the Chang Kang professor in the School of Chemistry and Chemical Engineering, NJU. His research interests include the metal-based anticancer complexes, fluorescent sensors for biorelated metal cations, and metal-based artificial nucleases and proteases.

Notes and references

[a] *State Key Laboratory of Coordination Chemistry, Coordination Chemistry, School of Chemistry and Chemical Engineering, Nanjing University, Nanjing 210093, P. R. China. Fax: +86 25 83314502; Tel: +86 25 83597066; +86 25 83621193. E-mail: heweij69@nju.edu.cn, zguo@nju.edu.cn.*

1 M. de Onis, E. A. Frongillo, M. Blçssner, *Bull. W. H. O.*, 2000, **78**, 1222.
2 A.I. Bush, *Curr. Opin. Chem. Biol.*, 2000, **4**, 184.
3 W.Maret, and Y.Li, *Chem. Rev.*, 2009, **109**, 4682.
4 C. J. Frederickson, J.-Y.Koh and A. I. Bush, *Nat. Rev. Neurosci.*, 2005, **6**, 449.
5 C. G. Taylor, *Biometals*, 2005, **18**, 305.
6 L. C. Costello and R. B. Franklin, *Mol. Cancer*, 2006, **5**, 17.
7 A.Krężel and W. Maret, *J. Biol. Inorg. Chem.*, 2006, **11**, 1049.
8 A.Krężel, Q. Hao and W. Maret, *Arch. Biochem. Biophys.*, 2007, **463**, 188.
9 Y. Chen, Y. Irie, W.M. Keung and W. Maret, *Biochemistry*, 2002, **41**, 8360.
10 D. J. Eide, *Biochim. Biophys. Acta,* 2006, **1763**, 711.
11 R. J. Cousins, J. P. Liuzzi and L. A. Lichten, *J. Biol. Chem.*, 2006, **281**, 24085.
12 B. Y. Kong, F. E. Duncan, E. L. Que, A. M. Kim, T. V. O'Halloran and T. K. Woodruff, *Mol. Hum. Reprod.*, 2014, **20**, 1077.
13 K. J. Waldron, J. C. Rutherford, D. Ford and N. J. Robinson, *Nature*, 2009, **460**, 823.
14 C. E. Outten and T. V. O'Halloran, *Science*, 2001, **292**, 2488.
15 A. J. Bird, K. McCall, M. Kramer, E. Blankman, D. R. Winge and D. J. Eide, *EMBO J.*, 2003, **22**, 5137.
16 L. Zhu, Z. Yuan, J. T. Simmons and K. Sreenath, *RSC Adv.*, 2014, **4**, 20398.
17 R. B. Franklin and L. C. Costello, *J. Cell Biochem.*, 2009, **106**, 750.
18 W. Maret, *Biometals*, 2009, **22**, 149.
19 A. Q. Truong-Tran, J. Carter, R.E. Ruffin and P. D. Zalewski, *Biometals*, 2001, **14**, 315.
20 S. J. Lippard and J. M. Berg, *Principles of Bioinorganic Chemistry*, University Science Books, Mill Valley, 1994.
21 G.K. Andrews, *Biometals*, 2001, **14**, 223.
22 G. Dodson and D. Steiner, *Curr. Opin. Struct. Biol.*, 1998, **8**, 189.
23 C. J. Frederickson, S. W. Suh, D. Silva, C. J. Frederickson and R. B. Thompson, *J. Nutr.*, 2000, **130**, 1471S.
24 S. C. Burdette and S. J. Lippard, *Coord. Chem. Rev.*, 2001, **216**, 333.
25 S. L. Sensi, P. Paoletti, A. I. Bush and I. Sekler, *Nat. Rev. Neurosci.*, 2009, **10**, 780.
26 P. Paoletti, A. M. Vergnano, B. Barbour and M. Casado, *Neuroscience*, 2009, **158**, 126.
27 Y. Li, C. J. Hough, C. J. Frederickson and J. M. Sarvey, *J. Neurosci.*, 2001, **21**, 8015.
28 J. M. Berg and Y. Shi, *Science*, 1996, **271**, 1081.
29 J. M. Berg and H. A. Godwin, *Annu. Rev. Biophys. Biomol. Struct.*, 1997, **26**, 357.
30 J.E. Coleman, *Curr. Opin. Chem. Biol.*, 1998, **2**, 222.
31 J. E. Coleman, *Annu. Rev. Biochem.*, 1992, **61**, 897.
32 B. L. Vallee and D. S. Auld, *Acc. Chem. Res.*, 1993, **26**, 543.
33 W. N. Lipscomb and N. Sträter, *Chem. Rev.*, 1996, **96**, 2375.
34 A. I. Bush, W. H. Pettingell, G. Multhaup, M. dParadis, J. P. Vonsattel, J. F. Gusella, K. Beyreuther, C. L. Masters and R. E. Tanzi, *Science*, 1994, **265**, 1464.
35 M. P. Cuajungco and G. J. Lees, *Neurobiol. Dis.*, 1997, **4**, 137.
36 A. I. Bush and R. E. Tanzi, *Proc. Natl. Acad. Sci. U.S.A.*, 2002, **99**, 7317.
37 R. Lobinski, C. Moulin, and R. Ortega, *Biochimie*, 2006, **88**, 1591.
38 J. Goldschmidt, W. Zuschratter and H. Scheich, *Neuroimage*, 2004, **23**, 638.
39 R. McRae, P. Bagchi, S. Sumalekshmy and C. J. Fahrni, *Chem. Rev.*, 2009, **109**, 4780.
40 P. Jiang and Z. Guo, *Coord. Chem. Rev.*, 2004, **248**, 205.
41 R. B. Thompson, *Curr. Opin. Chem. Biol.*, 2005, **9**, 526.
42 Z. Xu, J. Yoon and D. R. Spring, *Chem. Soc. Rev.*, 2010, **39**, 1996.
43 R. J. Radford and S. J. Lippard, *Curr. Opin. Chem. Biol.*, 2013, **17**, 129.
44 M. D. Pluth, E. Tomat and S. J. Lippard, *Annu. Rev. Biochem.*, 2011, 80, 333.
45 E. L. Que, D. W. Domaille and C. J. Chang, *Chem. Rev.*, 2008, **108**, 1517.
46 N. C. Lim, H. C. Freake and C. Brückner, *Chem. -Eur. J.*, 2005, **11**, 38.
47 P. Carol, S. Sreejith and A. Ajayaghosh, *Chem. Asian J.*, 2007, **2**, 338.
48 J. Cheon and J. H.Lee, *Acc. Chem. Res.*, 2008, **41**, 1630.
49 J. L. Major, G. Parigi, C. Luchinat and T. J. Meade, *Proc. Natl. Acad. Sci. U. S. A.*, 2007, **104**, 13881.
50 X. A. Zhang, K. S. Lovejoy, A. Jasanoff and S. J. Lippard, *Proc. Natl. Acad. Sci., U. S. A.*, 2007, **104**, 10780.
51 A. C. Esqueda, J. A. Lopez, G. Andreu-de-Riquer, J. C. Alvarado-Monzon, J. Ratnakar, A. J. M. Lubag, A. D. Sherry and L. M. De Leon-Rodriguez, *J. Am. Chem. Soc.*, 2009, **131**, 11387.
52 (a) E. L. Que, C. J. Chang, *Chem. Soc. Rev.*, 2010, **39**, 51; (b) L. De Leon-Rodriguez, A. J. M. Lubag Jr., A D. Sherry, *Inorg. Chim. Acta,* 2012, **393**, 12.
53 L. Schermelleh, R. Heintzmann, and H. Leonhardt, *J. Cell Biol.*, 2010, **190**, 165.
54 J. A. Conchello and J. W. Lichtman, *Nat. Methods*, 2005, **2**, 920.
55 T. Walter, D. W. Shattuck, R. Baldock, M. E. Bastin, A. E. Carpenter, S. Duce, J. Ellenberg, A. Fraser, N. Hamilton, S. Pieper, M. A. Ragan, J. E. Schneider, P. Tomancak and J. K. Hériché, *Nat. Methods*, 2010, **7**, s26.
56 F. Wang and X. Liu, *Chem. Soc. Rev.*, 2009, **38**, 976.
57 G. Hong, J. C. Lee, J. T. Robinson, U. Raaz, L. Xie, N. F. Huang, J. P. Cooke, and H. Dai, *Nat. Med.*, 2012, **18**, 1841.
58 J. Pichaandi and F. C. J. M. van Veggel, *Coord. Chem. Rev.*, 2014, **263-264**, 138.

59 P. D. Zalewski, I. J. Forbes and W. H. Betts, *Biochem. J.*, 1993, **296**, 403.
60 P. D. Zalewski, S. H. Millard, I. J. Forbes, O. Kapaniris, A. Slavotinek, W. H. Betts, A. D. Ward, S. F. Lincoln and I. Mahadevan, *J. Histochem. Cytochem.*, 1994, **42**, 877.
61 C. J. Frederickson, E. J. Kasarskis, D. Ringo and R. E. Frederickson, *J. Neurosci. Methods*, 1987, **20**, 91.
62 P. Coyle, P. D. Zalewski, J. C. Philcox, I. J. Forbes, A. D. Ward, S.F. Lincoln, I. Mahadevan and A.M. Rofe, *Biochem. J.*, 1994, **303**, 781.
63 P. D. Zalewski, I. J. Forbes, R. F. Seamark, R. Borlinghaus, W. H. Betts, S.F. Lincoln and A.D. Ward, *Chem. Biol.*, 1994, **1**, 153.
64 G. K. Walkup, S. C. Burdette, S. J. Lippard and R. Y. Tsien, *J. Am. Chem. Soc.*, 2000, **122**, 5644.
65 T. Hirano, K. Kikuchi, Y. Urano, T. Higuchi and T. Nagano, *J. Am. Chem. Soc.*, 2000, **122**, 12399.
66 T. Hirano, K. Kikuchi, Y. Urano and T. Nagano, *J. Am. Chem. Soc.*, 2002, **124**, 6555.
67 R. P. Haugland, *Handbook of Fluorescent Probes and Research Products*, 9th ed., Molecular Probes, Inc.: Eugene, OR, 2002.
68 K. R. Gee, Z. L. Zhou, D. Ton-That, S. L. Sensi and J. H. Weiss, *Cell Calcium*, 2002, **31**, 245.
69 E. M. Nolan and S. J. Lippard, *Acc. Chem. Res.*, 2009, **42**, 193.
70 K. Kikuchi, H. Komatsu and T. Nagano, *Curr. Opin. Chem. Biol.*, 2004, **8**, 182.
71 K. Komatsu, K. Kikuchi, H. Kojima, Y. Urano and T. Nagano, *J. Am. Chem. Soc.*, 2005, **127**, 10197.
72 A. Q. Truong-Tran, R. E. Ruffin, and P. D. Zalewski, *Am. J. Physiol. Lung Cell Mol. Physiol.* **2000**, *279*, L1172.
73 W.-J. Qian, K. R. Gee and R. T. Kennedy. *Anal. Chem.* **2003**, *75*, 3468.
74 K. R. Gee, Z.-L. Zhou, W.-J. Qian and R. Kennedy. *J. Am. Chem. Soc.* 2002, **124**, 776.
75 C. J. Chang, E. M. Nolan, J. Jaworski, S. C. Burdette, M. Sheng and S. J. Lippard, *Chem. Biol.*, 2004, **11**, 203.
76 E. M. Nolan and S. J. Lippard, *Inorg. Chem.*, 2004, **43**, 8310.
77 E. M. Nolan, J. W. Ryu, J. Jaworski, R. P. Feazell, M. Sheng and S. J. Lippard, *J. Am. Chem. Soc.*, 2006, **128**, 15517.
78 Y. Wu, X. Peng, B. Guo, J. Fan, Z. Zhang, J. Wang, A. Cui and Y. Gao, *Org. Biomol. Chem.*, 2005, **3**, 1387.
79 J. Wang, Y. Xiao, Z. Zhang, X. Qian, Y. Yang and Q. Xu, *J. Mater. Chem.*, 2005, **15**, 2836.
80 A. R. Kay and K. Tóth, *J. Neurophysiol.*, 2006, **95**, 1949.
81 G. Zhang, H. Li, S. Bi, L. Song, Y. Lu, L. Zhang, J. Yu and L. Wang, *Analyst*, 2013, **138**, 6163.
82 N. C. Lim, J. V. Schuster, M. C. Porto, M. A. Tanudra, L. Yao, H. C. Freake, C. Brückner, *Inorg. Chem.*, 2005, **44**, 2018.
83 S. Mizukami, S. Okada, S. Kimura and K. Kikuchi, *Inorg. Chem.*, 2009, **48**, 7630.
84 Y. Zhang, X. Guo, W. Si, L. Jia and X Qian, *Org. Lett.*, 2008, **10**, 473.
85 S. Maruyama, K. Kikuchi, T. Hirano, Y. Urano and T. Nagano, *J. Am. Chem. Soc.*, 2002, **124**, 10650.
86 C. J. Chang, J. Jaworski, E. M. Nolan, M. Sheng and S. J. Lippard, *Proc. Natl. Acad. Sci. U. S. A.*, 2004, **101**, 1129.
87 C. C. Woodroofe and S. J. Lippard, *J. Am. Chem. Soc.*, 2003, **125**, 11458.
88 C. C. Woodroofe, A. C. Won and S. J. Lippard, *Inorg. Chem.*, 2005, **44**, 3112.
89 Y. Qin, P. J. Dittmer, J. G. Park, K. B. Jansen and A. E. Palmer, *Proc. Natl. Acad. Sci. U. S. A.*, 2011, **108**, 7351.
90 L. H. Lindenburg, A. M. Hessels, E. H. T. M. Ebberink, R. Arts and M. Merkx, *ACS Chem. Biol.*, 2013, **8**, 2133.
91 P. J. Dittmer, J. G. Miranda, J. A. Gorski and A. E. Palmer, *J. Biol. Chem.*, 2009, **284**, 16289.
92 J. L. Vinkenborg, T. J. Nicolson, E. A. Bellomo, M. S. Koay, G. A. Rutter and M. Merkx, *Nat. Methods*, 2009, **6**, 737.
93 S. R. Adams, A. T. Harootunian, Y. J. Buechler, S. S. Taylor and R. Y. Tsien, *Nature*, 1991, **349**, 694.
94 K. Kikuchi, *Chem. Soc. Rev.*, 2010, **39**, 2048.
95 E. M. W. M. van Dongen, L. M. Dekkers, K. Spijker, E. W. Meijer, L. W. J. Klomp and M. Merkx, *J. Am. Chem. Soc.*, 2006, **128**, 10754.
96 E. M. W. M. van Dongen,T. H. Evers, L. M. Dekkers, E. W. Meijer, L. W. J. Klomp and M. Merkx, *J. Am. Chem. Soc.*, 2007, **129**, 3494.
97 M. M. Henary, Y. Wu and C. J. Fahrni, *Chem. -Eur. J.*, 2004, **10**, 3015.
98 Y. Xu and Y. Pang, *Chem. Commun.*, 2010, **46**, 4070.
99 Y. Xu, Q. Liu, B. Dou, B. Wright, J. Wang, and Y. Pang, *Adv. Healthcare Mater.*, 2012, **1**, 485.
100 Z. Liu, W. He and Z. Guo, *Chem. Soc. Rev.*, 2013, **42**, 1568.
101 K. P. Carter, A. M. Young, and A. E. Palmer, *Chem. Rev.*, 2014, **114**, 4564.
102 J. Wu, W. Liu, J. Ge, H. Zhang and P. Wang, *Chem. Soc. Rev.*, 2011, **40**, 3483.
103 F. W. J. Teale and G. Weber, *Biochem. J.*, 1957, **65**, 476.
104 J. M. Menter, *Photochem. Photobiol. Sci.*, 2006,**5**, 403.
105 R. Weissleder, *Nat. Biotechnol.*, 2001, **19**, 316.
106 Z. Guo, S. Park, J. Yoon and I. Shin, *Chem. Soc. Rev.*, 2014, **43**, 16.
107 A. R. Sarkar,D. E. Kang,H. M. Kimand B. R. Cho, *Inorg. Chem.*, 2014, **53**, 1794.
108 K. Kiyose, H. Kojima, Y. Urano and T. Nagano, *J. Am. Chem. Soc.*, 2006, **128**, 6548.
109 B. Tang, H. Huang, K. Xu, L. Tong, G. Yang, X. Liu and L. An, *Chem. Commun.*, 2006, 3609.
110 J. Cao, C. Zhao, X. Wang, Y. Zhang and W. Zhu, *Chem. Commun.*, 2012, **48**, 9897.
111Q. Q. Zhang, B. X. Yang, R. Sun, J. F. Ge, Y. J. Xu, N. J. Li and J. M. Lu, *Sensor. Actuat. B-Chem.*, 2012,**171**, 1001.
112 Y. Koide, Y. Urano, K. Hanaoka, T. Terai and T. Nagano,*ACS Chem. Biol.*, 2011, **6**, 600.
113 M. Fu, Y. Xiao, X. Qian, D. Zhao and Y. Xu, *Chem. Commun.*,2008, 1780.
114 T. Egawa, K. Hanaoka, Y. Koide, S. Ujita,N. Takahashi, Y. Ikegaya, N. Matsuki, T. Terai, T. Ueno,T. Komatsu and T. Nagano, *J. Am. Chem. Soc.*, 2011,**133**, 14157.
115 W. Denk, J. H. Strickler and W.W. Webb, *Science*, 1990, **248**, 73.
116 F. Helmchen and W. Denk, *Nat. Methods*, 2005, **2**, 932.
117 R. M. Williams, W. R. Zipfel and W. W. Webb, *Curr. Opin. Chem. Biol.*, 2001, **5**, 603.
118 S. Sumalekshmy and C. J. Fahrni, *Chem. Mater.*, 2011, **23**, 483.
119 H. M. Kim and B. R. Cho, *Acc. Chem. Res.*, 2009, **42**, 863.
120 M. Taki, J. L. Wolford and T. V. O'Halloran, *J. Am. Chem. Soc.*, 2004, **126**, 712.
121 R. G. Marvin, J. L. Wolford, M. J. Kidd, S. Murphy, J. Ward, E. L. Que, M. L. Mayer, J. E. Penner-Hahn, K. Haldar and T. V. O'Halloran, *Chem. Biol.*, 2012, **19**, 731.
122 X. Meng, S. Wang, Y. Li, M. Zhu and Q. Guo, *Chem. Commun.*, 2012, **48**, 4196.
123 X.-Y. Chen, J. Shi, Y.-M. Li, F.-L. Wang, X. Wu, Q. -X. Guo and L. Liu, *Org. Lett.*, 2009, **11**, 4426.
124 K. Suhling, P. M. W. French and D. Phillips, *Photochem. Photobiol. Sci.*, 2005, **4**, 13.
125 M. Y. Berezin and S. Achilefu, *Chem. Rev.*, 2010, **110**, 2641.
126 H. Brismar and B. Ulfhake, *Nat. Biotechnol.*, 1997, **15**, 373.
127 J. R. Lakowicz, in *Principles of Fluorescence Spectroscopy*, Springer, New York, 3rd edn., 2006, 756.
128 C. Hille, M. Lahn, H. G. Löhmannsröben, and C. Dosche, *Photochem. Photobiol. Sci.* 2009, **8**, 319.
129 J. R. Lakowicz, H. Szmacinski, R. B. Thompson, *Fluorescence lifetime-based sensing: applications to clinical chemistry and cellular imaging*. In: G. E. Cohn, editor. SPIE Conference on Ultrasensitve Laboratory Diagnostics, vol. 2388. Los Angeles, CA: SPIE, 1993, 2.
130 R. B. Thompson, D. Peterson, W. Mahoney, M. Cramer, B. P. Maliwal, S. W. Suh, C. Frederickson, C. Fierke and P. Herman, *J. Neurosci. Methods*, 2002, **118**, 63.
131 C. G. Morgan, A. C. Mitchell and J. G. Murray, *Proc. R. Microsc. Soc.*, 1990, **1**, 463.

132 I. Bugiel, K. König and H. Wabnitz, *Lasers Life Sci.*, 1989, **3**, 47.
133 J. R. Lakowicz, H. Szmacinski, K. Nowaczyk and M. L. Johnson, *Cell Calcium*, 1992, **13**, 131.
134 J. R. Lakowicz, H. Szmacinski, K. Nowaczyk and W. J. Lederer, *Cell Calcium*, 1994, **15**, 7.
135 B. Herman, P. Wodnicki, S. Kwon, A. Periasamy, G. W. Gordon, N. Mahajan and X. F. Wang, *J. Fluoresc.*, 1997, **7**, 85.
136 R. Sanders, H. C. Gerritsen, A. Draaijer, P. M. Houpt and Y. K. Levine, *Bioimaging*, 1994, **2**, 131.
137 E. Baggaleya, J. A. Weinsteina and J.A. G. Williams, *Coord. Chem. Rev.*, 2012, **256**, 1762.
138 K. Hanaoka, K. Kikuchi, S. Kobayashi, and T. Nagano, *J. Am. Chem. Soc.*, 2007, **129**, 13502.
139 Y. You, S. Lee, T. Kim, K. Ohkubo, W. Chae, S. Fukuzumi, G. Jhon, W. Nam and S. J. Lippard, *J. Am. Chem. Soc.*, 2011, **133**, 18328.
140 H. Woo, S. Cho, Y. Han, W. Chae, D. Ahn, Y. You and W. Nam, *J. Am. Chem. Soc.*, 2013, **135**, 4771.
141 K. Hanaoka, K. Kikuchi, H. Kojima, Y. Urano and T. Nagano, *J. Am. Chem. Soc.*, 2004, **126**, 12470.
142 Z. Ye, G. Wang, J. Chen, X. Fu, W. Zhang, J. Yuan, *Biosens. Bioelectron.*, 2010, **26**, 1043.
143 H. Haase, and D. Beyersmann, *Biochem. Biophys. Res. Commun.,* 2002, **296**, 923.
144K. Emmerson and K. Roehrig, *Comp. Biochem. Physiol., B: Biochem. Mol. Biol.*, 1992, **103**, 663.
145 Y.-L. P. Ow, D. R. Green, Z.Hao and T. W. Mak, *Nat. Rev. Mol. Cell Biol.*, 2008, **9**, 532.
146 M. P. Murphy and R. A. J. Smith, *Adv. Drug. Deliv. Rev.*, 2000, **41**, 235.
147 F. Pierrel, P. A. Cobine and D. R. Winge, *BioMetals*, 2007, **20**, 675.
148 A. Atkinson and D. R. Winge, *Chem. Rev.*, 2009, **109**, 4708.
149 S. Sensi, D. Ton-That, P. G. Sullivan, E. A. Jonas, K. R. Gee, L. K. Kaczmarek and J. H. Weiss, *Proc. Natl. Acad. Sci. U. S. A.*, 2003, **100**, 6157.
150 A. T. Hoye, J. E. Davoren, P. Wipf, M. P. Fink and V. E. Kagan, *Acc. Chem. Res.*, 2008, **41**, 87.
151 S. L. Sensi, D. Ton-That, J. H. Weiss, A. Rothe and K. R. Gee, *Cell Calcium*, 2003, **34**, 281.
152 M. P. Murphy, *Trends Biotechnol.*, 1997, **15**, 326.
153 B. C. Dickinson, D. Srikun and C. J. Chang, *Curr. Opin. Chem. Biol.*, 2010, **14**, 50.
154 W. Chyan, D. Y. Zhang, S. J. Lippard and R. J. Radford, *Proc. Natl. Acad. Sci. U. S. A.*, 2014, **111**, 143.
155 G. Masanta, C. S. Lim, H. J. Kim, J. H. Han, H. M. Kim and B. R. Cho, *J. Am. Chem. Soc.*, 2011, **133**, 5698.
156 N. Y. Baek, C. H. Heo, C. S. Lim, G. Masanta, B. R. Cho and H. M. Kim, *Chem. Commun.*, 2012, **48**, 4546.
157 L. Xue, G. Li, C. Yu and H. Jiang, *Chem.Eur. J.*, 2012, **18**, 1050.
158 K. Sreenath, J. R. Allen, M. W. Davidson and L. Zhu, *Chem. Commun.*, 2011, **47**, 11730.
159 Z. Liu, C. Zhang, Y. Chen, W. He and Z. Guo, *Chem. Commun.*, 2012, **48**, 8365.
160 J. J. Hwang, S.-J. Lee, T.-Y. Kim, J. -H. Cho and J.-Y. Koh, *J. Neurosci.,* **2008**, *28*, 3114.
161 F. Liu, T. Wu, J. Cao, S. Cui, Z. Yang, X. Qiang, S. Sun, F. Song, J. Fan, J. Wang and X. Peng, *Chem. Eur. J.*, 2013, **19**, 1548.
162 Y. Chen, C. Zhu, Z. Yang, J. Chen, Y. He, Y. Jiao, W. He, L. Qiu, J. Cen and Z. Guo, *Angew. Chem. Int. Ed.*, 2013, **52**, 1688.
163 J. G. Park, Y. Qin, D. F. Galati and A. E. Palmer, *ACS Chem. Biol.*, 2012, **7**, 1636.
164 A. Keppler, S. Gendreizig, T. Gronemeyer, H. Pick, H. Vogel and K. Johnsson, *Nat. Biotechnol.*, 2003, **21**, 86.
165 N. C. Shaner, G. H. Patterson and M. W. Davidson, *J. Cell Sci.*, 2007, **120**, 4247.
166 E. Tomat, E. M. Nolan, J. Jaworski and S. J. Lippard, *J. Am. Chem. Soc.*, 2008, **130**, 15776.
167 J. P. Luzio, P. R. Pryor and N. A. Bright, *Nat. Rev. Mol. Cell Biol.*, 2007, **8**, 622.
168 H. C. Roh, S. Collier, J. Guthrie, J. D. Robertson and K. Kornfeld, *Cell Metab.*, 2012, **15**, 88.
169 E. C. Freundt, M. Czapiga and M. J. Lenardo, *Cell Res.*, 2007, **17**, 956.
170 S. D. Goldman, R. S. Funk, R. A. Rajewski and J. P. Krise, *Bioanalysis*, 2008, **1**, 1445.
171 L. Xue, G. Li, D. Zhu, Q. Liu and H. Jiang, *Inorg. Chem.*, 2012, **51**, 10842.
172 H. Zhu, J. Fan, S. Zhang, J. Cao, K. Song, D. Ge, H. Dong, J. Wang and X. Peng, *Biomater. Sci.*, 2014, **2**, 89.
173 S. Iyoshi, M. Taki and Y. Yamamoto, *Org. Lett.*, 2011, **13**, 4558.
174 D. Li, S. Chen, E. A. Bellomo, A. I. Tarasov, C. Kaut, G. A. Rutter and W.-h. Li, *Proc. Natl. Acad. Sci. U. S. A.*, 2011, **108**, 21063.
175 R. J. Radford, W. Chyan and S. J. Lippard, *Chem. Sci.*, 2013, **4**, 3080.
176 J. Jeong, J. M. Walker, F. Wang, J. G. Park, A. E. Palmer, C. Giunta, M. Rohrbach, B. Steinmann and D. J. Eide, *Proc. Natl. Acad. Sci. U. S. A.,* 2012, **109**, E3530.
177 J. J. M. Hoozemans and W. Scheper, *Int. J. Biochem. Cell Biol.,* 2012, **44**, 1295.
178 C. D. Ellis, C. W. MacDiarmid and D. J. Eide, *J. Biol. Chem.,* 2005, **280**, 28811.
179 W. Lin, D. Buccella and S. J. Lippard, *J. Am. Chem. Soc.*, 2013, **135**, 13512.
180 C. Andreini, L. Banci, I. Bertini and A. Rosato, *J. Proteome Res.*, 2006, **5**, 3173.
181 C. Andreini, L. Banci, I. Bertini and A. Rosato, *J. Proteome Res.*, 2006, **5**, 196.
182 L. M. T. Canzoniero, D. M. Turetsky and D. W. Choi, *J. Neurosci.*, 1999, **19**, RC31.
183 C. Zhang, Z. Liu, Y. Li, W. He, X. Gao and Z. Guo, *Chem. Commun.*, 2013, **49**, 11430.
184 E. B. Veale, D. O. Frimannsson, M. Lawler and T. Gunnlaugsson, *Org. Lett.*, 2009, **11**, 4040.
185 E. B. Veale and T. Gunnlaugsson, *J. Org. Chem.*, 2010, **75**, 5513.
186 K. Rathore, C. S. Lim, Y. Lee and B. R. Cho, *Org. Biomol. Chem.*, 2014, **12**, 3406.
187 J. G. Miranda, A. L. Weaver, Y. Qin, J. G. Park, C. I. Stoddard, M. Z. Lin and A. E. Palmer, *PLoS One*, 2012, **7**, e49371.
188 J.-Y. Lee, T. B. Cole, R. D. Palmiter, S. W. Suh and J.-Y. Koh, *Proc. Natl. Acad. Sci. U. S. A.*, 2002, **99**, 7705.
189 Y. Li, C. J. Hough, S. W. Suh, J. M. Sarvey and C. J. Frederickson, *J. Neurophysiol.*, 2001, **86**, 2597.
190 K. Komatsu, Y. Urano, H. Kojima and T. Nagano, *J. Am. Chem. Soc.,* 2007, **129**, 13447.
191 C. J. Chang, E. M. Nolan, J. Jaworski, K. Okamoto, Y. Hayashi, M. Sheng and S. J.Lippard, *Inorg. Chem.*, 2004, **43**, 6774.
192 H. M. Kim, M. S. Seo, M. J. An, J. H. Hong, Y. S. Tian, J. H. Choi, O. Kwon, K. J. Lee and B. R. Cho, *Angew. Chem., Int. Ed.*, 2008, **47**, 5167.
193 I. A. Danish, C. S. Lim, Y. S. Tian, J. H. Han, M. Y. Kang and B. R. Cho, *Chem. -Asian J.*, 2011, **6**, 1234.
194 C. Huang, J. Qu, J. Qi, M. Yan and G. Xu, *Org. Lett.*, 2011, **13**, 1462.
195 M. Khana, C. R. Goldsmithb, Z. Huang, J. Georgioua, T. T. Luybena, J. C. Rodera, S. J. Lippard and K. Okamoto, *Proc. Natl. Acad. Sci. U. S. A*, 2014, **111**, 6786.
196 K. P. Divya, S. Sreejith, P. Ashokkumar, K. Yuzhan, Q. Peng, S. K. Maji, Y. Tong, H. Yu, Y. Zhao, P. Ramamurthy and A. Ajayaghosh, *Chem. Sci.*, 2014, **5**, 3469.
197 S.-K. Ko, X. Chen, J. Yoon and I. Shin, *Chem. Soc. Rev.*, 2011, **40**, 2120.
198 F. Qian, C. Zhang, Y. Zhang, W. He, X. Gao, P. Hu and Z. Guo, *J. Am. Chem. Soc.*, 2009, **131**, 1460.
199 Z. Xu, K.-H. Baek, H. N. Kim, J. Cui, X. Qian, D. R. Spring, I. Shin and J. Yoon, *J. Am. Chem. Soc.*, 2010, **132**, 601.
200 J. E. Kwon, S. Lee, Y. You, K.-H. Baek, K. Ohkubo, J. Cho, S. Fukuzumi, I. Shin, S. Y. Park and W. Nam, *Inorg. Chem.*, 2012, **51**, 8760.

201 K. Jobe, C. H. Brennan, M..Motevalli, S. M. Goldup and M. Watkinson, *Chem. Commun.*, 2011, **47**, 6036.
202 Z. Liu, C. Zhang, Y. Chen, F. Qian, Y. Bai, W. He, Z. Guo, *Chem. Commun.*, 2014, **50**, 1253.
203 Z. Guo, G.-H. Kim, I. Shin and J. Yoon, *Biomaterials*, 2012, **33**, 7818.
204 Z. Guo, G.-H. Kim, J. Yoon and I. Shin, *Nat. Protoc*., 2014, **9**, 1245.
205 T. F. Massoud and S. S. Gambhir, *Genes Dev.*, 2003, **17**, 545.
206 S. K. Ghosh, P. Kim, X. A. Zhang, S. H. Yun, A. Moore, S. J. Lippard and Z. Medarova, *Cancer Res.*, 2010, **70**, 6119.
207 J. Zhou, Z. Liu and F. Li, *Chem. Soc. Rev.,* 2012, **41**, 1323.
208 H. H. Gorris and O. S. Wolfbeis, *Angew. Chem., Int. Ed.*, 2013, **52**, 3584.
209 J. Peng, W. Xu, C. L. Teoh, S. Han, B. Kim, A. Samanta, J. C. Er, L. Wang, L. Yuan, X. Liu and Y.-T. Chang, *J. Am. Chem. Soc.*, 2015, DOI: 10.1021/ja5115248.
210 M. Fernández-Suárez and A. Y. Ting, *Nat. Rev. Mol. Cell Bio.,* 2008, **9**, 929.
211 B. Huang, M. Bates and X. Zhuang, *Annu. Rev. Biochem.,* 2009, **78**, 993.

